Check for updates

Advanced Materials

ADVANCED MATERIALS
www.advmat.de

REVIEW

Unlocking the Potential of Magnesium-Based Hydrogen Storage Composites via Advanced Thermodynamic and Kinetic Tuning Strategies

Yingyan Zhao[1,2] | Yinghui Li[1,2] | Bolun Wang[1,2] | Xi Lin[1,2] | Zhigang Hu[1,2] | Ji Nie[1,2,3] | Boyang Mao[4] | Wenjiang Ding[1,2] | Andrea C. Ferrari[4] | Jianxin Zou[1,2,4,5]

[1]National Engineering Research Center of Light Alloy Net Forming & State Key Laboratory of Metal Matrix Composites, Shanghai Jiao Tong University, Shanghai, P. R. China | [2]Center of Hydrogen Science, Shanghai Jiao Tong University, Shanghai, P. R. China | [3]The third Research Laboratory, Sinopec Research Institute of Petroleum Processing Co., Ltd, Beijing, P. R. China | [4]Cambridge Graphene Centre, University of Cambridge, Cambridge, UK | [5]School of Materials Science and Engineering, Inner Mongolia University of Science and Technology, Baotou, P. R. China

Correspondence: Andrea C. Ferrari (acf26@eng.cam.ac.uk) | Jianxin Zou (zoujx@sjtu.edu.cn)

Received: 28 August 2026 | **Revised:** 23 October 2026 | **Accepted:** 29 October 2026

Keywords: Solid-state hydrogen storage | Magnesium hydride | Thermodynamic and kinetic tuning | System integration | Machine learning

ABSTRACT

The development of efficient and safe solid-state hydrogen storage technologies is pivotal for the transition toward sustainable clean energy. Magnesium is a promising hydrogen carrier due to its high gravimetric (7.6 wt.% for MgH_2) and volumetric storage capacity (110 kg m^{-3}), abundance, and excellent reversibility. However, the practical application of Mg-based materials is hindered by their high thermodynamic stability ($\Delta H = -74.7$ kJ mol^{-1} H_2) and sluggish sorption kinetics. Here, we overview the latest advances in Mg-based composites for high hydrogen storage performance. We discuss key material modification strategies, including catalysis, nanostructuring, alloying, and external field assistance to tune the thermodynamic and kinetic properties of Mg-based materials. We stress the emerging role of machine learning in accelerating material design, performance prediction, and optimization. We also critically assess the techno-economic viability of Mg-based hydrogen storage within integrated hydrogen value chains. This assessment considers how storage connects with hydrogen production, transport, and end-use applications. Finally, we outline challenges and future research directions, aiming to guide the rational design of next-generation Mg-based hydrogen storage materials and systems toward commercial applications.

1 | Introduction

Growing energy consumption leads to excessive fossil fuel consumption, which aggravates global environmental degradation [1]. This has emerged as a critical societal concern and drives the development of sustainable energy solutions [2]. In recent years, an increasing number of countries have been raising the share of renewable energy in their national energy mix. This is achieved through measures such as developing renewable energy industries, establishing national emission reduction targets, and promoting key technologies such as carbon capture [3], utilization [4], and storage (Carbon Capture, Utilization and Storage, CCUS) [5]. These efforts aim to reduce reliance on fossil fuels (Figure 1a). Hydrogen energy is extensively regarded as one of the most promising solutions for addressing the energy crisis and achieving sustainability in the 21st century [6, 7]. Hydrogen is abundant in chemically bound forms, particularly in water and organic compounds, but molecular hydrogen must be produced using an external energy source [8]. It should therefore be regarded as an energy carrier rather than a primary

All rights reserved, including rights for text and data mining and training of artificial intelligence technologies or similar technologies.
© 2026 Wiley-VCH GmbH

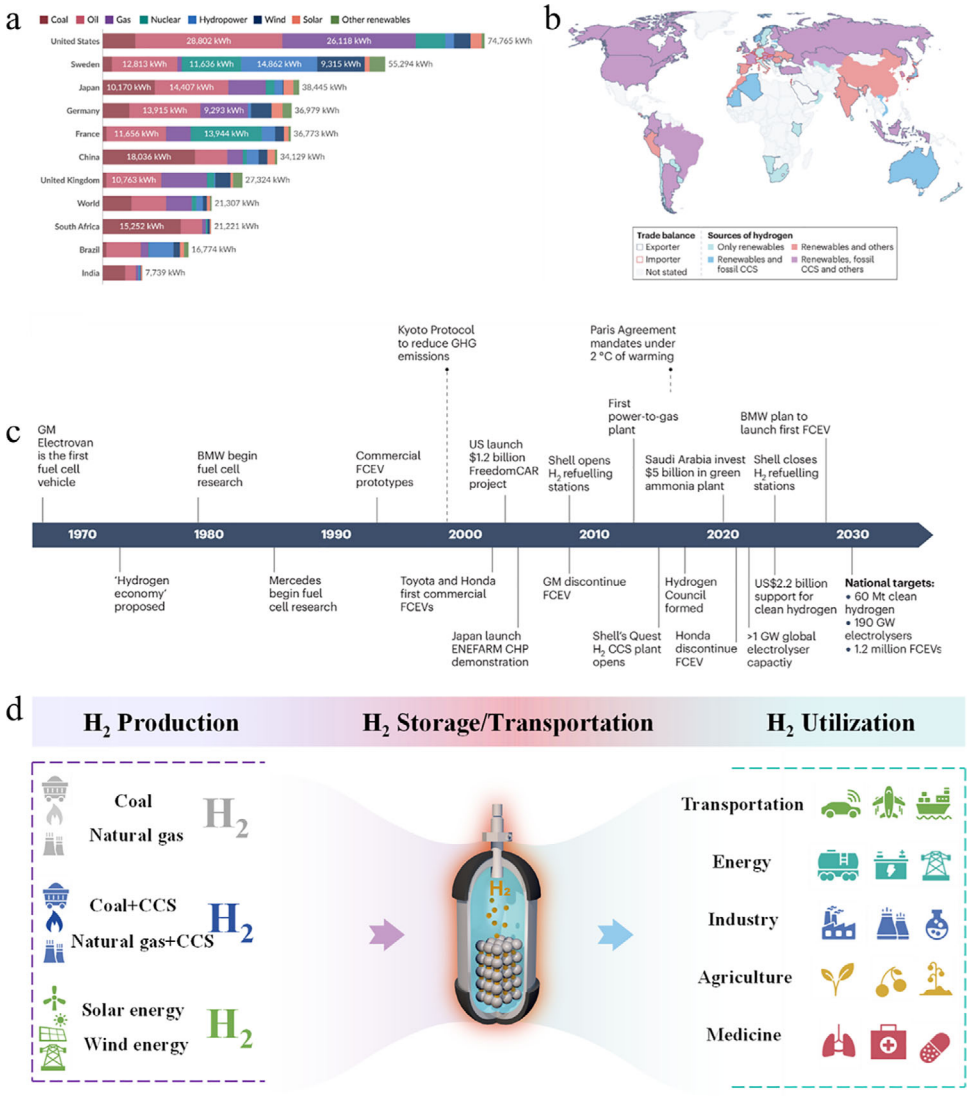


FIGURE 1 | (a) Per capita primary energy consumption by source in 2024. Data obtained from Our World in Data. (b) Countries and regions with national hydrogen strategies. Fill colors indicate the supported hydrogen sources, while border colors indicate whether the countries plan to become hydrogen exporters or importers. (c) Timeline of selected milestones in the development of hydrogen energy. Adapted with permission [10]. Copyright 2025, Springer Nature. (d) Schematic illustration of the hydrogen supply chain, including hydrogen production, storage and transportation, and end use.

or intrinsically renewable energy source. When produced using low-carbon processes, H_2 can facilitate the decarbonization of sectors that are difficult to electrify directly and can store energy generated from intermittent renewable sources. Its chemical energy is released through combustion or electrochemical oxidation, producing water when H_2 reacts with oxygen. H_2 also possesses high gravimetric energy densities, with lower and higher heating values of approximately 120 and 142 MJ kg^{-1}, respectively. However, its low volumetric energy density under ambient conditions creates substantial challenges for storage and transportation [9].

Since 2017, national hydrogen strategies have been announced by 65 countries, reflecting growing policy support for domestic and international hydrogen value chains (Figure 1b) [10]. These strategies commonly associate hydrogen development with industrial decarbonization, energy security, job creation, technological innovation, and economic diversification [11]. The United States, the European Union, Japan, and China are expected to account for more than 80% of the announced global hydrogen supply by 2030, although the realization of these targets will depend on infrastructure development, investment, and sustained policy support [12–14]. The underlying vision can be traced to the concept of the "hydrogen economy", popularized by John Bockris in the 1970s (Figure 1c) [10]. In this framework, low-carbon hydrogen production is connected to storage and transportation infrastructure and, ultimately, to its use in industry, mobility, power generation, and other end-use sectors (Figure 1d). Hydrogen storage and transportation therefore constitute the critical link between geographically and temporally distributed production and demand [15]. The maturity and viability of these technologies determine the feasibility of large-scale and commercial H_2 utilization. H_2 has inherent physico-chemical properties, such as low volumetric energy density, high diffusivity, embrittlement effects, and high flammability, posing significant challenges for safe and cost-effective storage and transportation. H_2 storage

15214095, 0, Downloaded from https://advanced.onlinelibrary.wiley.com/doi/10.1002/adma.75618 by Cambridge University Library, Wiley Online Library on [05/11/2026]. See the Terms and Conditions (https://onlinelibrary.wiley.com/terms-and-conditions) on Wiley Online Library for rules of use; OA articles are governed by the applicable Creative Commons License

methods can be mainly divided into 3 categories: gaseous-state, liquid-state, and solid-state, with different storage tanks [16].

2 | Fundamentals of Magnesium-Based Hydrogen Storage

Figure 2a compares the gravimetric hydrogen capacities and estimated operating temperatures of representative hydrogen storage materials [17]. Among these candidates, metal hydrides offer a compelling combination of high volumetric hydrogen density (110 kg/m^3 for MgH_2), low-pressure operation, and reversible hydrogen uptake and release, making them attractive for stationary storage and selected transportation applications [18]. Their reversible exothermic hydrogenation and endothermic dehydrogenation reactions also enable coupling with thermal-management and energy-conversion systems. However, practical performance depends not only on intrinsic hydrogen capacity but also on reaction thermodynamics, sorption kinetics, heat transfer, cycling stability, and system-level mass and volume. Magnesium hydride (MgH_2) has been extensively investigated because magnesium is abundant and comparatively inexpensive, while MgH_2 possesses a theoretical gravimetric hydrogen capacity of 7.6 wt.% and a high volumetric hydrogen density [19, 20]. It also exhibits a high theoretical thermal energy storage density of 2814 kJ kg^{-1} [21]. MgH_2 achieves reversible H_2 storage and release through the following chemical reaction Equation (1).

$$Mg + H_2 \leftrightarrow MgH_2 \tag{1}$$

The formation of MgH_2 from Mg and H_2 has a standard enthalpy change of approximately -75 kJ mol^{-1} H_2; equivalently, its dehydrogenation requires an enthalpy input of approximately +75 kJ mol^{-1} H_2 [22]. This large reaction enthalpy reflects the strong thermodynamic stability of MgH_2 and results in an equilibrium hydrogen pressure of approximately 1 bar only at temperatures near 280°C–300°C [23]. The Mg-H interaction has mixed ionic and covalent character, and hydrogen release requires Mg-H bond cleavage followed by the diffusion and recombination of hydrogen atoms to form H_2 [24]. First-principles calculations have reported substantial energy barriers for individual bond-breaking or surface-reaction steps, although these microscopic barriers should not be equated directly with experimentally determined apparent activation energies [25]. Hydrogenation is likewise a multistep process involving H_2 adsorption and dissociation at the Mg surface, hydrogen incorporation, hydride nucleation and growth, and hydrogen transport through the Mg/MgH_2 phases. Slow H_2 dissociation on pristine Mg surfaces and limited hydrogen diffusion, particularly through MgH_2, therefore impose additional kinetic constraints. The practical operating temperature of the Mg/MgH_2 system is consequently determined by the combined effects of equilibrium thermodynamics, interfacial reaction kinetics, and heat and mass transfer [26].

2.1 | The Thermodynamic Principles

The equilibrium thermodynamics of MgH_2 and related Mg-based hydrides are commonly evaluated using pressure-composition-temperature measurements. A pressure composition isotherm, abbreviated as PCI, records the equilibrium hydrogen pressure as a function of hydrogen concentration at a fixed temperature. A series of PCI curves measured at different temperatures constitutes a pressure composition temperature dataset, abbreviated as PCT. These measurements provide the plateau pressure, reversible capacity, hysteresis, and phase boundaries of the metal hydride system. At low hydrogen concentrations, dissociated hydrogen atoms occupy interstitial sites in metallic Mg and form a hydrogen poor α solid solution (Figure 2b) [27]. As the hydrogen pressure increases, the hydrogen rich β-MgH_2 phase nucleates and grows. Coexistence of the α and β phases produces a pressure plateau. Its slope and width can be affected by compositional heterogeneity, elastic strain, particle size, hysteresis, and incomplete equilibration. Plateau pressures measured at different temperatures can be analyzed using the van't Hoff equation (Equation 2) to determine the standard enthalpy and entropy changes of hydrogenation, ΔH_{hyd} and ΔS_{hyd}, respectively [28].

$$\ln\left(\frac{P_{eq}}{P^0}\right) = \frac{\Delta H_{hyd}}{RT} - \frac{\Delta S_{hyd}}{R} \tag{2}$$

Here, P_{eq} is the equilibrium hydrogen pressure, and P^0 is the standard pressure, typically 1 bar. ΔH_{hyd} and ΔS_{hyd} are the standard enthalpy and entropy changes for the hydrogenation reaction $Mg + H_2 \rightarrow MgH_2$, respectively. Both quantities are negative under standard conditions. R is the universal gas constant, 8.314 J mol^{-1} K^{-1}, and T is the absolute temperature in kelvin. Using reported thermodynamic parameters, the equilibrium hydrogen pressure of the Mg/MgH_2 system is approximately 0.07 bar at 200°C [29]. Hydrogen cannot be delivered above this pressure at equilibrium, regardless of the intrinsic reaction kinetics. A higher operating temperature or a lower outlet pressure is therefore required to provide sufficient thermodynamic driving force for dehydrogenation. Vacuum assistance can increase this driving force, but it also introduces auxiliary energy consumption and additional system complexity.

2.2 | The Kinetic Principles

The equilibrium hydrogen pressure of MgH_2 is approximately 1 bar at 280°C [30]. In practice, its onset desorption temperature can exceed 300°C because hydrogen release remains kinetically hindered. The temperature dependence of the apparent reaction rate parameter is commonly described by the Arrhenius equation (Equation 3) [31]:

$$k\ (T) = Ae^{\frac{-E_a}{RT}} \tag{3}$$

where $k(T)$ is the temperature-dependent rate constant associated with the selected kinetic model, A is the pre-exponential factor, E_a is the apparent activation energy. The exponential dependence of $k(T)$ on E_a indicates that the reaction rate can be increased either by raising the temperature or by introducing pathways with lower kinetic barriers. However, E_a derived from temperature-dependent sorption measurements is an apparent parameter that may incorporate several elementary and transport processes rather than the barrier of a single Mg-H bondbreaking event. Moreover, the Arrhenius relation describes the temperature dependence of the rate constant but does not itself account for the thermodynamic driving force, which depends on the difference

15214095, 0, Downloaded from https://advanced.onlinelibrary.wiley.com/doi/10.1002/adma.75618 by Cambridge University Library, Wiley Online Library on [05/11/2026]. See the Terms and Conditions (https://onlinelibrary.wiley.com/terms-and-conditions) on Wiley Online Library for rules of use; OA articles are governed by the applicable Creative Commons License

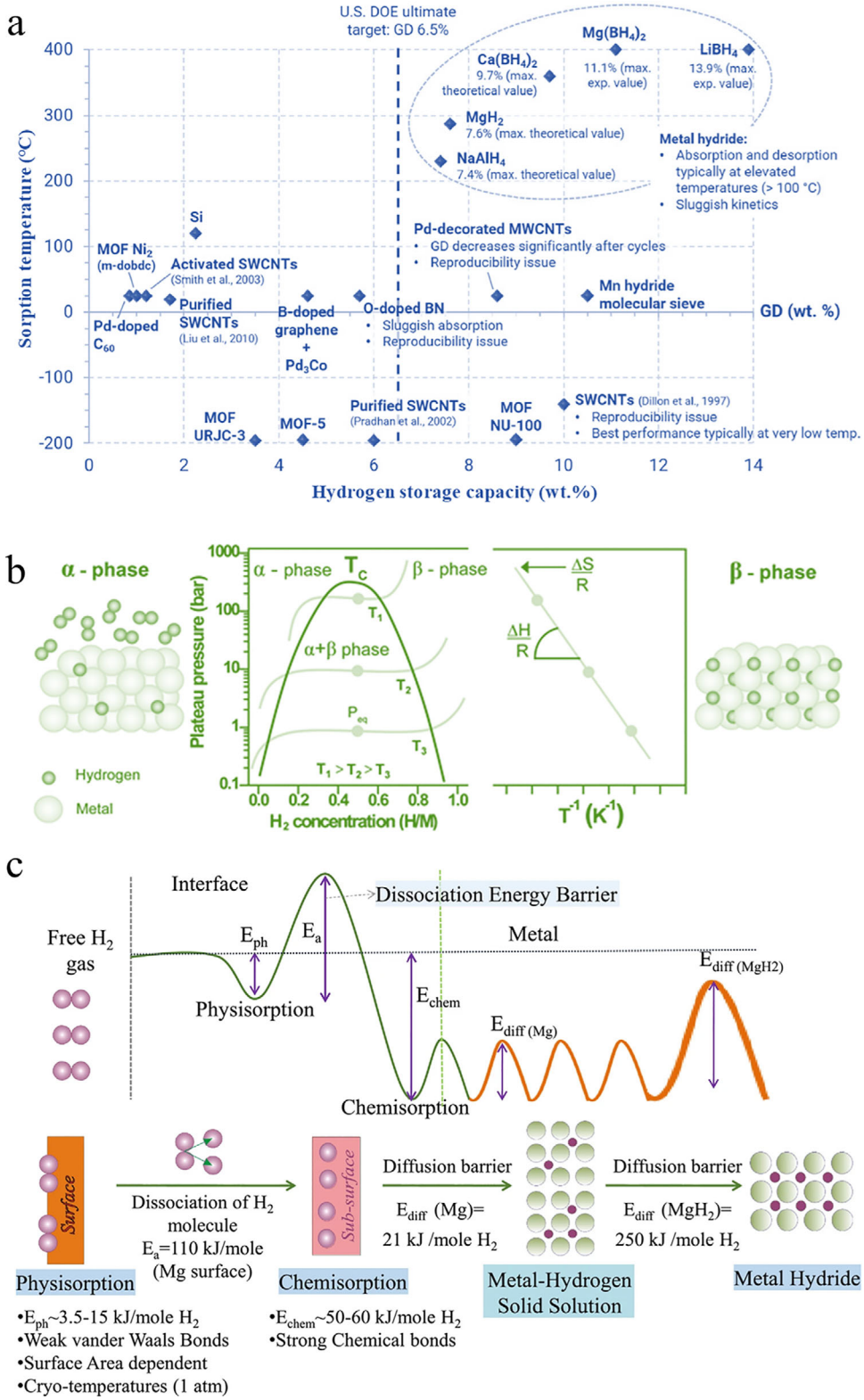


FIGURE 2 | (a) Gravimetric hydrogen capacities and estimated operating temperatures of representative hydrogen storage materials. Adapted with permission [17]. Copyright 2023, Elsevier. (b) Pressure-composition isotherms and the corresponding van't Hoff plot for the phase transition between a metal α phase and a metal hydride β phase. The reaction enthalpy and entropy can be derived from the slope and intercept of the van't Hoff plot. Adapted with permission [27]. Copyright 2011, The Royal Society of Chemistry. (c) Schematic potential energy profile and representative energy barriers for hydrogen absorption and desorption in metals, including the reported values for Mg. Adapted with permission [32]. Copyright 2021, Elsevier.

15214095, 0, Downloaded from https://advanced.onlinelibrary.wiley.com/doi/10.1002/adma.75618 by Cambridge University Library, Wiley Online Library on [05/11/2026]. See the Terms and Conditions (https://onlinelibrary.wiley.com/terms-and-conditions) on Wiley Online Library for rules of use; OA articles are governed by the applicable Creative Commons License

between the applied hydrogen pressure and the equilibrium pressure determined from the PCT and van't Hoff analyses.

As for Figure 2c, hydrogenation of Mg includes 4 main steps: 1) H_2 physisorption on the Mg surface; 2) H_2 dissociation on the Mg surface; 3) H chemisorption into the Mg lattice; 4) H atoms diffusion in the MgH_2 bulk [32]. Each is associated with a distinct free-energy barrier, and the rate-controlling step may change with temperature, hydrogen pressure, conversion fraction, particle size, surface chemistry, and catalyst addition. Although the gas-phase H-H bond dissociation energy is approximately 432 kJ mol^{-1}, this value should not be interpreted as the activation barrier for H_2 dissociation on Mg [33]; the relevant surface barrier depends on the adsorption configuration and the chemical state of the Mg surface. After dissociation, hydrogen transport can become increasingly restrictive as MgH_2 forms because hydrogen diffusivity in the hydride phase is substantially lower than that in metallic Mg. Reported diffusion coefficients are strongly dependent on temperature, phase composition, defect density, and measurement method; representative values are on the order of 10^{-11} m^2 s^{-1} in Mg and can decrease to approximately 10^{-18} m^2 s^{-1} in MgH_2 under the reported conditions [34, 35].

The location and morphology of hydride nucleation further determine the dominant transport pathway. When MgH_2 nucleates predominantly within Mg particles, hydrogen transport through the metallic matrix may contribute substantially to the overall rate [36]. By contrast, surface nucleation can produce a relatively dense MgH_2 shell around an unreacted Mg core, progressively shifting the kinetic limitation toward hydrogen transport across the hydride layer. The experimentally derived E_a therefore represents the combined response of interfacial reactions, nucleation and growth, and phase-dependent hydrogen transport, and its physical interpretation requires an appropriate kinetic model and information about the microstructural evolution of the material [37].

3 | Multiscale Strategies for Tuning Mg-Based Hydrogen Storage Materials

As discussed above, the operating behavior of Mg-based hydrides is governed by two distinct but coupled constraints: the equilibrium thermodynamics of the MgH_2/Mg reaction and the kinetic barriers associated with surface reactions, nucleation, phase growth, and hydrogen transport. The high thermodynamic stability of MgH_2 limits the equilibrium hydrogen pressure at moderate temperatures, whereas sluggish reaction kinetics can shift the practical absorption and desorption conditions even further from equilibrium. Materials engineering must therefore distinguish strategies that alter the free-energy landscape from those that primarily accelerate the approach to equilibrium.

Current approaches include catalytic modification, nanostructuring and nanoconfinement, alloying, and external-field assistance. These strategies act through different mechanisms and should not be evaluated solely by reductions in onset desorption temperature. Catalysts and reduced diffusion lengths predominantly improve kinetics, whereas alloy formation and sufficiently strong nanoscale or interfacial effects may also modify reaction thermodynamics. In all cases, improvements in reaction rate or operating temperature must be considered together with reversible capacity, cycling stability, additive mass, oxidation resistance, manufacturability, and system-level heat and mass transfer. The following sections assess the mechanisms, performance gains, and inherent trade-offs of these complementary approaches.

3.1 | Catalytic Doping

Catalytic additives used in Mg-based hydrogen storage materials include carbonaceous materials (graphene [38], porous carbon [39]), transition metals/transition-metal compounds (oxides [40, 41], halides [42, 43], carbides [44, 45], nitrides [46, 47], and hydrides [48, 49]). Their catalytic behavior cannot be attributed to a single universal electronic feature. Instead, their activity depends on their ability to promote one or more elementary processes, including H_2 adsorption and dissociation, hydrogen recombination, interfacial hydrogen transfer, and the nucleation of Mg or MgH_2. For transition-metal-containing catalysts, partially occupied d states can facilitate interactions with H_2 and thereby reduce the barriers to dissociation or recombination [50, 51]. The effectiveness of this interaction depends on the identity, oxidation state, coordination environment, and dynamic evolution of the catalytic phase during hydrogen cycling.

Catalyst/Mg interfaces can provide preferential sites for heterogeneous nucleation and establish alternative pathways for hydrogen transfer. Hydrogen transport through certain metallic catalyst phases can also be substantially faster than transport through MgH_2, potentially allowing these phases to function as local hydrogen-transfer pathways. However, comparisons of diffusion coefficients across different materials require caution because the mobile species, temperature range, crystal structure, and measurement method may differ. More broadly, catalytic additives primarily accelerate the rate at which the Mg/ MgH_2 system approaches equilibrium; unless they induce the reversible formation of a new thermodynamic phase or a substantial interfacial free-energy contribution, they do not intrinsically change the equilibrium pressure of the Mg/ MgH_2 reaction. High-energy ball milling is widely used to incorporate catalytic additives into Mg-based materials [52]. In addition to dispersing the catalyst, milling reduces particle and crystallite sizes, creates defects and fresh interfaces, and can partially disrupt surface oxide layers. Consequently, the performance improvement observed after ball milling cannot always be assigned exclusively to the chemical activity of the catalyst. Appropriate control samples are required to separate catalytic effects from changes in particle size, defect density, surface condition, and phase composition.

Several mechanisms have been proposed to explain catalyst-assisted hydrogen sorption, including hydrogen spillover [53], surface/interface reactions [54], the hydrogen pump effect [55], and electron transfer between catalytic phases of different valence states [56]. It is worth noting that the "hydrogen pump" concept is often invoked to explain faster hydrogen sorption in metal hydrides, although direct experimental evidence of the proposed hydrogen transfer remains difficult to obtain. These descriptions are useful mechanistic models, but their applicability depends on direct evidence for the identity and evolution of the active phase. In situ or operando characterization, isotope-tracing measurements, and calculations of complete interfacial reaction

15214095, 0, Downloaded from https://advanced.onlinelibrary.wiley.com/doi/10.1002/adma.75618 by Cambridge University Library, Wiley Online Library on [05/11/2026]. See the Terms and Conditions (https://onlinelibrary.wiley.com/terms-and-conditions) on Wiley Online Library for rules of use; OA articles are governed by the applicable Creative Commons License

pathways are therefore needed to distinguish among competing mechanisms. The practical value of a catalyst should ultimately be assessed by the magnitude and durability of its kinetic enhancement relative to the penalties introduced by additive mass, capacity loss, cost, structural coarsening, and chemical instability during cycling.

3.1.1 | Multicomponent Metal-Based Catalysts

Single-component metal-based catalysts can accelerate hydrogen sorption in Mg-based composites by promoting surface reactions, interfacial hydrogen transfer, or hydride nucleation [57–61]. More recent studies have increasingly focused on multicomponent catalysts, in which chemically distinct phases may perform complementary functions [62–64]. Such systems can generate heterogeneous interfaces, facilitate the dispersion of active species, and establish alternative pathways for hydrogen transport. Their apparent advantages, however, should not be interpreted simply as the additive contributions of the individual components. Ball milling and hydrogen cycling can induce phase decomposition, reduction, alloying, and hydride formation, meaning that the active catalyst may differ substantially from the initially added precursor. Moreover, reductions in onset desorption temperature or apparent activation energy primarily indicate kinetic enhancement and do not necessarily imply a change in the equilibrium thermodynamics of MgH_2.

For example, a YF_3-Ni/C precursor generated YH_2/YH_3, Mg_2Ni/Mg_2NiH_4, and MgF_2 during processing and cycling, while the carbon support maintained the dispersion of these phases [43]. The resulting MgH_2 composite exhibited an onset desorption temperature of 221.1°C, an apparent activation energy of 74.56 kJ mol^{-1}, and 98.4% capacity retention after 30 cycles (Figure 3a). A similar transformation occurred in MgH_2 modified with reduced graphene oxide supported VS_4 (rGO@VS_4). Reaction-derived V species and MgS-containing interfaces were associated with faster hydrogen exchange and less particle coarsening [65]. This composite achieved an onset desorption temperature of 180°C and an apparent activation energy of ~63.8 kJ mol^{-1} (Figure 3b), although the 15 wt.% catalyst loading imposed a substantial capacity penalty. At a finer structural scale, a PdNi bimetallene precursor reconstructed into alloy clusters, compositionally segregated clusters, and atomically dispersed species during processing and cycling [66]. The working-state PdNi clusters were correlated with d-band-mediated promotion of hydrogen exchange, enabling an onset desorption temperature of 149°C (Figure 3c).

These examples distinguish precursor composition, reaction-derived phases, and sites that function during a particular hydrogen sorption step. Phase evolution has been identified in the YF_3-Ni/C, rGO@VS_4, and PdNi systems, although the individual contributions of coexisting species remain partly inferred. These studies indicate that the performance of multicomponent catalysts is governed less by the nominal precursor composition than by the phases, interfaces, and electronic structures established under operating conditions. Catalytic enhancement can arise from the coupling of H_2 dissociation and recombination, interfacial hydrogen transfer, heterogeneous nucleation, charge redistribution, and structural stabilization. Establishing causal relationships nevertheless requires operando identification of the active phases and carefully designed control experiments. Catalyst systems should therefore be compared using composite-level reversible capacity, catalyst loading, pressure and heating conditions, cycling durability, cost, and structural evolution. Onset temperature and apparent activation energy alone do not really provide a sufficient basis for comparison.

3.1.2 | Defect-Engineered Metal Oxide Catalysts

Metal oxide-based composites provide adaptable interfaces whose defect populations, oxidation states, and interactions with Mg can evolve during hydrogen cycling. Their role can also extend to resistance against air exposure when combined with alloying. Ding et al. [67] reported an MgSc-TiO_2 composite in which the α-Mg phase showed no detectable oxidation after six months in air, with only limited $MgSc_2O_4$ formation. The composite also exhibited a reversible hydrogen capacity of 5.86 wt.% at 320°C. Calculations suggested that electron buffering by Sc and competitive oxygen binding at Ti and Sc sites helped limit Mg oxidation, while evolving interfacial phases contributed to the improved sorption kinetics.

Sun et al. used phosphorus doping as an anion-modulation strategy to improve both the catalytic activity and cycling stability of Li_3VO_4 for MgH_2 (Figure 4a). Phosphorus incorporation increased the concentration of oxygen vacancies in the catalyst. Reversible changes in local V-P and V-V coordination were proposed to accommodate cycling-induced strain and preserve catalytically active V species. The authors described this self-regulating response as the "spring effect" [68]. The modified MgH_2 composite exhibited an onset desorption temperature of 214°C. At the atomic limit of catalyst dispersion, Ru single atoms supported on Nb_2O_5 ($Ru_{0.028}$@Nb_2O_5) modified the electronic and transport properties of the oxide support [69]. The reported 47-fold increase in electrical conductivity, together with multivalent Nb species and cycling-induced oxygen vacancies, was associated with apparent activation energies of 74.06 and 14.07 kJ mol^{-1} H_2 for dehydrogenation and rehydrogenation, respectively (Figure 4b). These values should nevertheless be interpreted in the context of the kinetic models and experimental ranges used for their derivation. Dynamic oxide-to-metal or oxide-to-hydride transformation provides an additional catalytic pathway. Oxygen-deficient H-V_2O_5 nanosheets generated V- and VH_2-containing species during processing and hydrogen cycling, coupling defect-rich interfaces with rapid hydrogen transfer through the reversible V/VH_2 transformation [70]. The resulting MgH_2 composite showed an onset desorption temperature of 185°C, absorbed 2.38 wt.% H_2 at 30°C under the reported pressure and time conditions, and retained approximately 99% of its reversible capacity over 100 cycles (Figure 4c). Although these results demonstrate favorable low-temperature kinetics and cycling stability, the room-temperature uptake represents only part of the available hydrogen capacity and should not, by itself, be interpreted as evidence of system-level practicality.

Taken together, these studies show that the catalytic response of metal oxide additives arises from evolving interactions among the oxide, Mg/MgH_2, and reaction-derived phases. Defects, changes

15214095, 0, Downloaded from https://advanced.onlinelibrary.wiley.com/doi/10.1002/adma.75618 by Cambridge University Library, Wiley Online Library on [05/11/2026]. See the Terms and Conditions (https://onlinelibrary.wiley.com/terms-and-conditions) on Wiley Online Library for rules of use; OA articles are governed by the applicable Creative Commons License

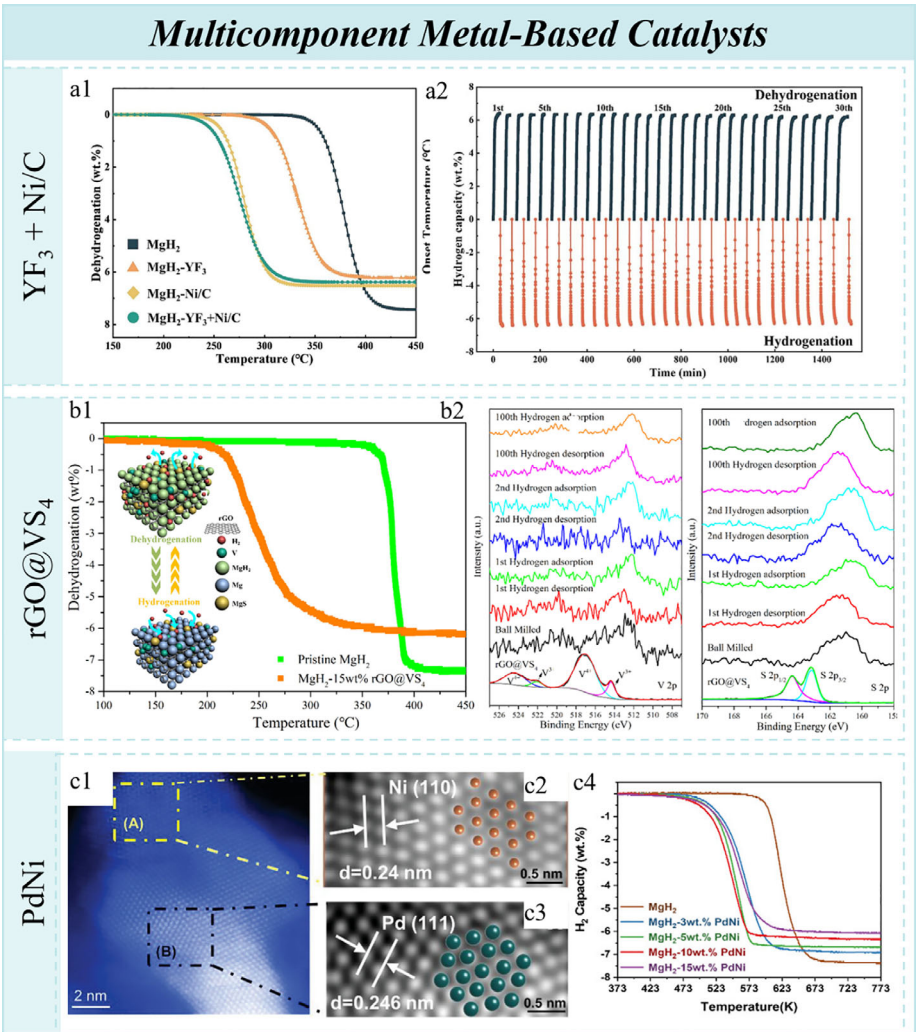


FIGURE 3 | Catalytic modification of MgH_2 using multicomponent metal-based catalysts. (a1, a2) Thermal desorption behavior and hydrogen absorption and desorption cycling performance of MgH_2-YF_3-Ni/C. Adapted with permission [43]. Copyright 2025, Elsevier. (b1, b2) Thermal desorption behavior and X-ray photoelectron spectra of MgH_2 containing 15 wt.% rGO@VS_4. Adapted with permission [65]. Copyright 2025, Elsevier. (c1-c4) HAADF-STEM images of the reaction-derived PdNi species and thermal desorption behavior of MgH_2 containing 10 wt.% PdNi and the corresponding control samples. Adapted with permission [66]. Copyright 2023, Wiley.

in metal coordination and oxidation state, and newly formed metallic or hydride species can reinforce one another during hydrogen cycling. The resulting interfaces can promote hydrogen activation and transfer while helping to retain catalytic activity, although their relative contributions differ among systems. Identifying the working-state interface is therefore more informative than describing the initial oxide alone. The role of oxygen vacancies should be considered alongside concurrent changes in phase composition, particle size, and interfacial structure. Comparisons should also consider catalyst loading, reversible composite-level capacity, cycling durability, and synthesis complexity.

3.2 | Nanostructuring and Nanoconfinement

Nanostructuring can accelerate hydrogen sorption in Mg-based materials by increasing the accessible surface area, shortening hydrogen-transport distances, and introducing grain boundaries, defects, and heterogeneous nucleation sites [71]. These effects primarily improve reaction kinetics. Changes in equilibrium thermodynamics may also arise when the characteristic dimensions become sufficiently small for surface or interfacial free energies to contribute appreciably to the total Gibbs free energy [72]. Such thermodynamic effects are generally expected to become pronounced only at the ultrasmall scale and should be distinguished from reductions in onset temperature caused by faster kinetics. Mg-based nanostructures have been prepared using vapor deposition [73], high-energy ball milling [74], solution-phase reduction [75], and confinement within nanoscale scaffolds [76]. Each method offers different control over particle size, interface chemistry, oxidation, aggregation, and scalability.

3.2.1 | Unsupported Nanostructures and Dimensional Control

Reducing the dimensions of Mg or MgH_2 increases the fraction of surface and interfacial atoms and decreases the characteristic

15214095, 0, Downloaded from https://advanced.onlinelibrary.wiley.com/doi/10.1002/adma.75618 by Cambridge University Library, Wiley Online Library on [05/11/2026]. See the Terms and Conditions (https://onlinelibrary.wiley.com/terms-and-conditions) on Wiley Online Library for rules of use; OA articles are governed by the applicable Creative Commons License

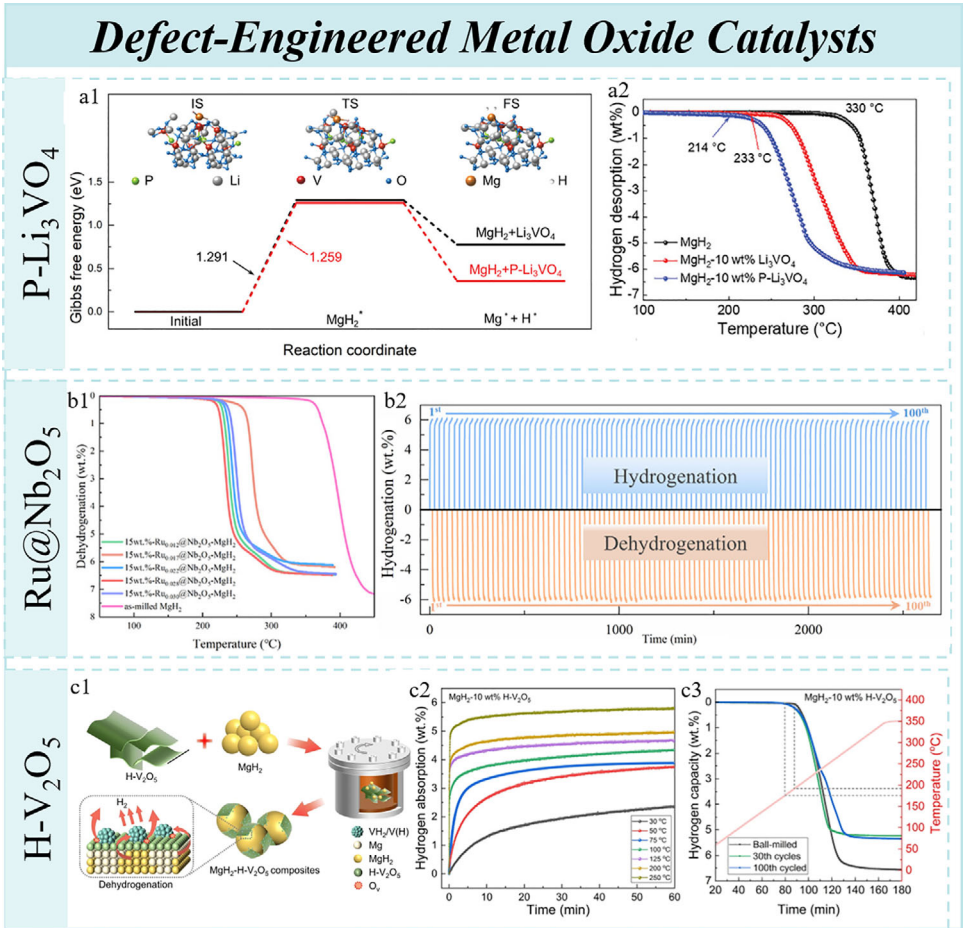


FIGURE 4 | Catalytic modification of MgH_2 using metal oxide-based catalysts. (a1, a2) Calculated hydrogen dissociation energy profiles and thermal desorption behavior of MgH_2-10 wt.% P-Li_3VO_4. Adapted with permission [68]. Copyright 2025, Wiley. (b1, b2) Thermal desorption behavior and hydrogen absorption and desorption cycling performance of MgH_2-15 wt.% $Ru_{0.028}@Nb_2O_5$. Adapted with permission [69]. Copyright 2025, Wiley. (c1-c3) Proposed dehydrogenation mechanism, isothermal hydrogen absorption behavior, and cyclic thermal desorption performance of MgH_2-10 wt.% H-V_2O_5. Adapted under the terms of the Creative Commons Attribution 4.0 International License [70]. Copyright 2024, Springer.

distance over which hydrogen must migrate. The resulting improvement in sorption kinetics can originate from faster surface exchange, shorter diffusion pathways, and a higher density of nucleation sites [77]. However, particle size, crystallite size, and diffusion length are not interchangeable quantities: a micrometre-scale particle may contain nanometre-scale crystallites, while oxide shells and particle agglomeration can restrict the accessible surface area.

At sufficiently small dimensions, differences between the surface free energies of Mg and MgH_2 can shift the equilibrium hydrogen pressure. For the dehydrogenation reaction $MgH_2 \rightarrow Mg + H_2$, the standard Gibbs free energy change of spherical nanoparticles can be approximated as Equation (4):

$$\Delta_r G^0_{nano} = \Delta_r G^0_{bulk} + \frac{3V_{Mg}\gamma_{Mg}}{r_{Mg}} - \frac{3V_{MgH_2}\gamma_{MgH_2}}{r_{MgH_2}} \quad (4)$$

and the corresponding equilibrium pressure is related to this free-energy change by Equation (5):

$$\ln\left(\frac{P_{eq,nano}}{P^0}\right) = -\frac{\Delta_r G^\circ_{nano}}{RT} \quad (5)$$

Here, $P_{eq,\,nano}$ is the equilibrium hydrogen pressure of the nanoscale system, and P^0 is the standard pressure. $\Delta_r G^0{}_{nano}$ is the standard Gibbs free energy change for the dehydrogenation reaction of nanoscale MgH_2 at temperature T. V_i, γ_i, and r_i are the molar volume, surface or interfacial energy, and particle radius of phase i, respectively. The subscript i denotes Mg or MgH_2. R is the universal gas constant, 8.314 J mol^{-1} K^{-1}, and T is the absolute temperature in kelvin.

Whether this contribution stabilizes or destabilizes MgH_2 depends on the relative surface energies and sizes of the Mg and MgH_2 phases; nanosizing does not inherently guarantee hydride destabilization. The equation also assumes spherical, monodisperse particles with well-defined surfaces and therefore provides an idealized thermodynamic description rather than a complete representation of aggregated or scaffold-confined materials. Calculations by Wagemans et al. [78] predicted that the thermodynamic stability of MgH_2 decreases markedly only for clusters below approximately 1.3 nm. A 0.9 nm MgH_2 cluster was estimated to correspond to a hydrogen-release temperature of approximately 200°C under the specified equilibrium conditions. This result illustrates the potential magnitude of finite-size effects, but such ultrasmall clusters contain a large

15214095, 0, Downloaded from https://advanced.onlinelibrary.wiley.com/doi/10.1002/adma.75618 by Cambridge University Library, Wiley Online Library on [05/11/2026]. See the Terms and Conditions (https://onlinelibrary.wiley.com/terms-and-conditions) on Wiley Online Library for rules of use; OA articles are governed by the applicable Creative Commons License

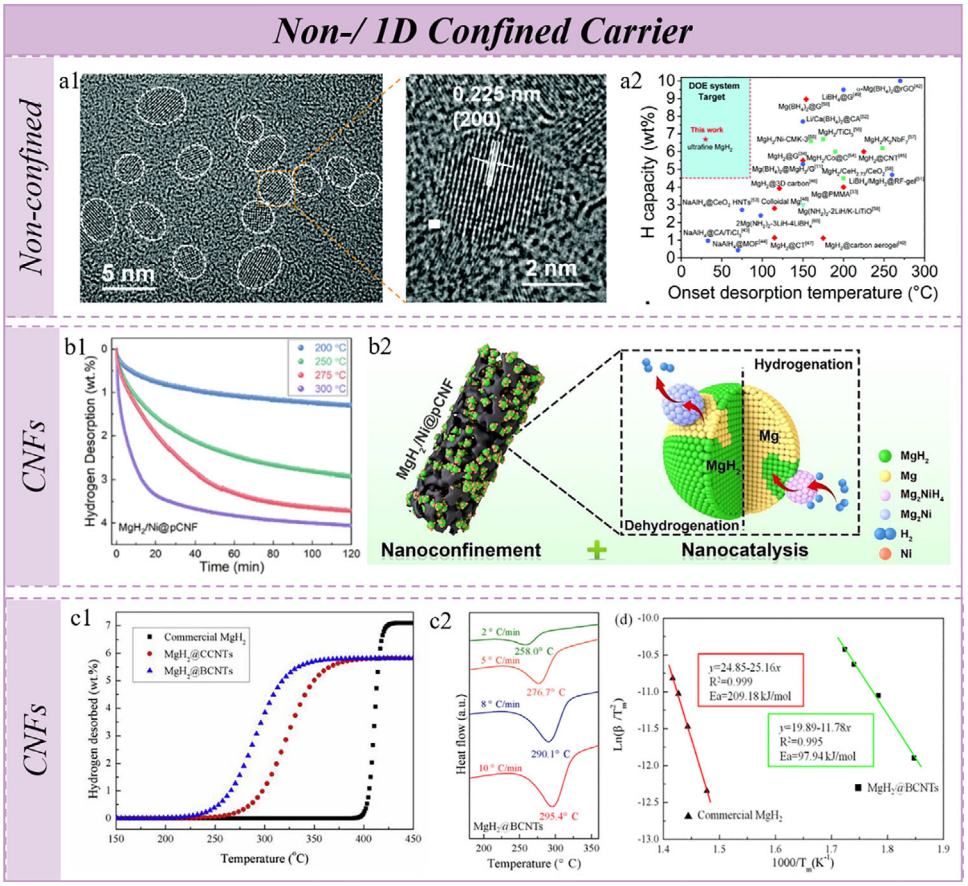


FIGURE 5 | Nanoscale modification of Mg-based hydrides using nonconfined and one-dimensional (1D) architectures. (a1, a2) HRTEM image and hydrogen storage performance comparison chart of nonconfined ultrafine Mg/ MgH_2 nanoparticles. Adapted with permission [80]. Copyright 2021, The Royal Society of Chemistry. (b1, b2) Isothermal hydrogen desorption behavior and proposed reaction mechanism of MgH_2/Ni@pCNF. Adapted with permission [81]. Copyright 2022, Elsevier. (c1-c3) Thermal desorption behavior, differential scanning calorimetry curves, and Kissinger analysis of MgH_2@BCNTs. Adapted with permission [82]. Copyright 2019, Elsevier.

fraction of surface atoms and may differ structurally from bulk crystalline MgH_2. Their predicted behavior should therefore not be extrapolated directly to MgH_2 particles or crystallites tens of nanometres in size. Experimental studies nevertheless show a clear size dependence of sorption kinetics at larger dimensions. Chemically reduced Mg nanocrystals with diameters of 25, 32, and 38 nm reached 95% of their respective hydrogen capacities at 300°C within approximately 60, 140, and 420 s, respectively [75]. Similarly, Mg nanowires with diameters of 30–50 and 80–100 nm released 3.28 and 2.65 wt.% H_2 within 30 min, compared with 0.5 wt.% for nanowires with diameters of 150–170 nm under the same conditions [79]. These results primarily demonstrate kinetic benefits arising from reduced dimensions rather than conclusive changes in equilibrium thermodynamics.

More pronounced thermodynamic and kinetic effects were reported for free-standing MgH_2 nanoparticles with diameters of approximately 4–5 nm prepared through an ultrasound-assisted solution route [80]. The nanoparticles began to release detectable hydrogen at 30°C and delivered up to 6.0 wt.% H_2 within 40 min at 85°C under the reported measurement conditions (Figure 5a). A van't Hoff analysis yielded a dehydrogenation enthalpy of 59.5 kJ mol^{-1} H_2, while apparent activation energies of 80 and 28 kJ mol^{-1} H_2 were reported for dehydrogenation and hydrogenation, respectively. Density functional theory calculations further suggested lower barriers for H_2 dissociation, hydrogen migration, and H_2 release in Mg clusters than on an extended Mg surface. These results point to strong finite-size effects, but their interpretation requires careful consideration of particle-size distributions, surface ligands, oxidation, aggregation, pressure conditions, and the establishment of equilibrium during thermodynamic measurements.

Overall, unsupported Mg and MgH_2 nanostructures provide clear kinetic advantages, whereas experimentally verified thermodynamic destabilization remains largely restricted to the ultrasmall-size regime. Their practical use is additionally constrained by oxidation sensitivity, particle coarsening, low packing density, and the difficulty of preserving nanoscale dimensions during repeated cycling. These limitations motivate the use of nanoconfinement and supporting frameworks discussed in the following sections.

Nanoconfinement restricts Mg or MgH_2 within nanoscale pores, channels, or interfacial domains. During synthesis, the scaffold can act as a nanoreactor that regulates nucleation, particle growth, and spatial distribution. During hydrogen cycling, it can suppress particle coarsening and preserve short

15214095, 0, Downloaded from https://advanced.onlinelibrary.wiley.com/doi/10.1002/adma.75618 by Cambridge University Library, Wiley Online Library on [05/11/2026]. See the Terms and Conditions (https://onlinelibrary.wiley.com/terms-and-conditions) on Wiley Online Library for rules of use; OA articles are governed by the applicable Creative Commons License

hydrogen-transport distances. The local chemical environment of the scaffold may additionally influence interfacial bonding, defect formation, and the identity of reaction-derived catalytic phases. Common scaffolds therefore combine high surface area and controlled porosity with sufficient thermal, chemical, and mechanical stability. Their performance nevertheless depends on pore accessibility, MgH_2 loading, scaffold mass, interfacial chemistry, and the ability to retain the confined structure during repeated phase transformations.

1D scaffolds provide elongated channels or hollow interiors that can restrict particle growth while maintaining connected pathways through the composite. Ren et al. confined approximately 15 nm MgH_2 nanoparticles and Ni-containing species within metal-organic-framework-derived porous carbon nanofibres, producing MgH_2/Ni@pCNF (Figure 5b) [81]. The composite began to release hydrogen at 200°C and completed dehydrogenation at 275°C under the reported conditions. Its kinetic and cycling behavior was attributed to the combined effects of particle confinement, N-containing interfacial sites, and Mg_2Ni/Mg_2NiH_4 phases formed during processing and cycling. The carbon framework limited particle coarsening, whereas the Ni-containing phases provided additional pathways for hydrogen exchange. Bamboo-like carbon nanotubes provide a related architecture in which internal compartments restrict MgH_2 growth. Liu et al. prepared 15–20 nm MgH_2 particles within such nanotubes, achieving a reported MgH_2 loading of 76.8 wt.% (Figure 5c) [82]. The relatively high loading reduced the capacity loss commonly associated with porous scaffolds, while the compartmentalized structure suppressed particle coalescence and may have accommodated cycling-induced strain. These examples show that the principal advantages of 1D scaffolds are the preservation of nanoscale particles and the formation of connected interfacial and transport networks. Claims of directional hydrogen diffusion or enhanced electronic conduction, however, require direct transport measurements because the effective pathway may be interrupted by closed pores, oxide layers, scaffold defects, or incomplete MgH_2 connectivity. Practical assessment must additionally consider scaffold mass, volumetric packing density, pore-filling efficiency, thermal conductivity, and the scalability of precursor infiltration.

2D materials can provide large interfacial areas for dispersing MgH_2 nanoparticles and limiting their lateral coarsening. Graphene-supported MgH_2 illustrates this approach: high-pressure solvothermal synthesis produced dispersed MgH_2 nanoparticles on graphene sheets with improved structural retention during cycling (Figure 6a) [83]. Graphene alone, however, generally provides limited catalytic activity for H_2 dissociation and recombination. Its tendency to restack can also reduce the accessible surface area and weaken the intended confinement effect. Functionalization or incorporation of additional catalysts can address these limitations but introduces further inactive mass, synthetic complexity, and possible changes in surface chemistry. MXenes offer a more chemically active alternative because their transition-metal centers, high conductivity, and tunable surface terminations can combine structural support with interfacial catalysis. Conventional ball milling may damage their layered architecture, motivating bottom-up assembly strategies that preserve accessible interfaces. Zhu et al. [84] constructed a wrinkled $Ti_3C_2T_x$-derived scaffold and anchored highly dispersed MgH_2 nanoparticles onto its surface through solution-phase assembly. Removal of oxygen-containing surface species before MgH_2 incorporation was intended to limit undesirable MgO formation. The resulting MgH_2@Ti-MX composite began to release hydrogen at 140°C, delivered 3.0 wt.% H_2 within 2.5 h at 150°C, and retained a reversible composite-level capacity of approximately 4.0 wt.% after 60 cycles (Figure 6b). Its behavior was attributed to the combined effects of nanoscale dispersion, MgH_2-scaffold heterointerfaces, and TiH_2-containing phases formed in situ. These results demonstrate favorable low-temperature kinetics, although the moderate composite capacity and multistep synthesis remain relevant constraints for scale-up. A related strategy used oxygen-vacancy TiO_2 nanosheets to combine interfacial anchoring with catalyst generation. Ren et al. [85] employed an $MgBu_2$ precursor to promote MgH_2 assembly while modifying the defect chemistry of the TiO_2 support, producing a flower-like MgH_2/ TiO_2 heterostructure. The composite began to release hydrogen at 180°C and exhibited an initial dehydrogenation rate of 2.116 wt.% min^{-1} at 300°C, together with 98.5% capacity retention after 100 cycles (Figure 6c). Oxygen vacancies and Mg—Ti—O interfacial phases were correlated with faster interfacial reactions, while the 2D support restricted particle coarsening. Collectively, 2D scaffolds can integrate particle stabilization with chemically active heterointerfaces, but their performance is governed by more than nominal dimensionality. Surface termination, restacking, pore accessibility, catalyst evolution, MgH_2 loading, and interface durability determine whether the nanoscale advantages persist during cycling. Comparisons should therefore report the capacity of the complete composite, scaffold fraction, equilibrium pressure, sorption conditions, particle-size evolution, and volumetric packing density. Without these metrics, a lower onset temperature alone cannot establish the practical advantage of a nanoconfined architecture.

2D supports combine physical confinement with different degrees of chemical activity. Carbon scaffolds mainly limit MgH_2 coarsening, whereas MXenes and defect-engineered oxides can also provide reactive interfaces through surface terminations, vacancies, and phases formed during cycling [86, 87]. Their practical value depends on preserving accessible interfaces at useful MgH_2 loadings without excessive capacity dilution. A lower onset temperature alone does not establish thermodynamic destabilization.

3.2.2 | Scaffold Design: Porous Templates and 3D Networks

3D porous scaffolds can confine Mg or MgH_2 within interconnected pores while providing mechanical support against particle coarsening and cycling-induced structural changes. Compared with lower-dimensional supports, they may offer higher loading capacities and more spatially distributed interfaces. Their influence on hydrogen and heat transport, however, depends on pore connectivity, tortuosity, scaffold composition, MgH_2 filling fraction, and interfacial contact; porosity alone does not guarantee rapid mass or heat transfer. Li et al. [88] incorporated MgH_2 into 3D Ni single-atom-doped porous carbon (Ni SA-pC), forming MgH_2@Ni SA-pC (Figure 7a). The composite exhibited an onset desorption temperature of 170°C. Ni atoms coordinated by four N atoms were proposed to induce interfacial charge

15214095, 0, Downloaded from https://advanced.onlinelibrary.wiley.com/doi/10.1002/adma.75618 by Cambridge University Library, Wiley Online Library on [05/11/2026]. See the Terms and Conditions (https://onlinelibrary.wiley.com/terms-and-conditions) on Wiley Online Library for rules of use; OA articles are governed by the applicable Creative Commons License

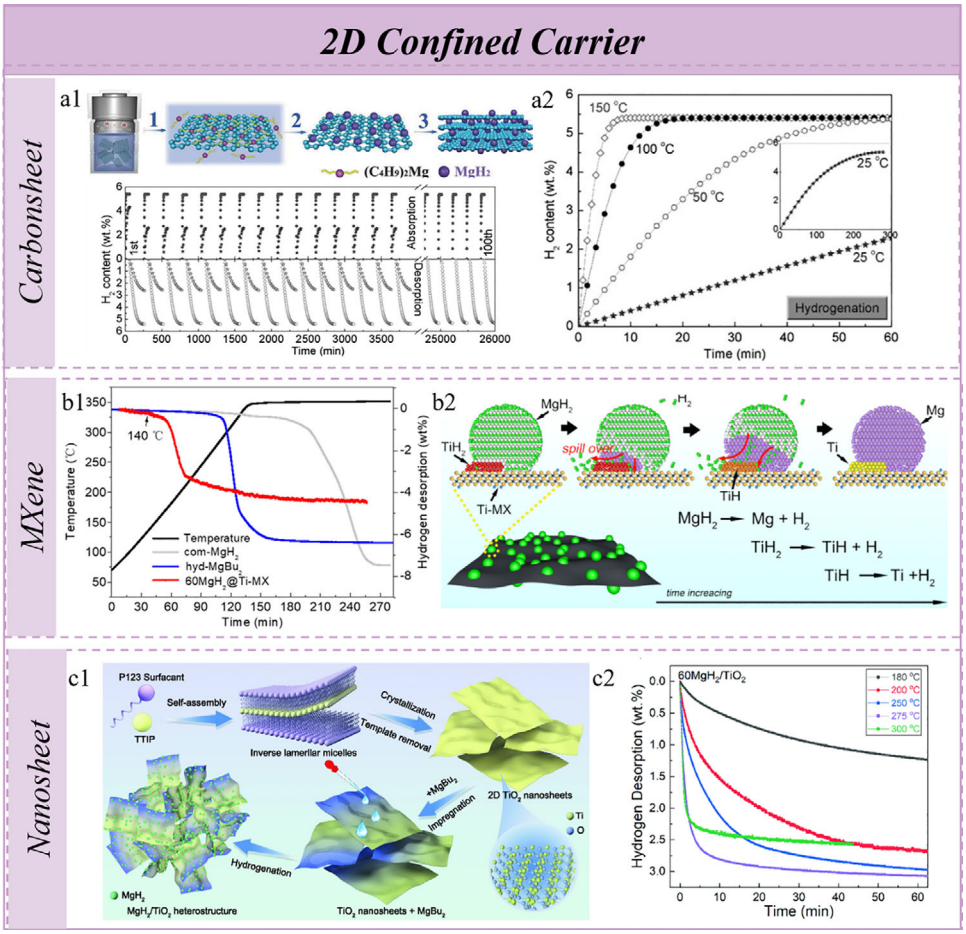


FIGURE 6 | Nanoconfinement of MgH_2 using 2D scaffolds. (a1, a2) Schematic preparation route, cycling performance, and isothermal hydrogen absorption behavior of MgH_2@Gr. Adapted with permission [83]. Copyright 2015, Wiley. (b1, b2) Thermal desorption behavior and proposed dehydrogenation mechanism of 60 MgH_2@Ti-MX. Adapted with permission [84]. Copyright 2021, American Chemical Society. (c1,c2) Schematic preparation route and isothermal hydrogen desorption behavior of MgH_2/TiO_2. Adapted under the terms of the Creative Commons Attribution 4.0 International License [85]. Copyright 2022, Springer.

redistribution and facilitate hydrogen exchange, while the porous carbon framework restricted MgH_2 coarsening. Calculations yielded an H_2 dissociation barrier of 1.33 eV for the modelled interface. The composite retained 94.4% of its initial capacity after 10 cycles, although substantially longer cycling is required to establish durability. Nitrogen-doped porous carbon provides a related platform without an added metal catalyst. A composite containing 60 wt.% MgH_2 confined within reduced N-doped porous carbon (MgH_2@rN-pC) combined reversible Mg/ MgH_2 chemistry with cryogenic hydrogen adsorption by the scaffold [89]. It adsorbed approximately 0.8 wt.% H_2 at -196°C and 3 MPa, began to desorb chemically stored hydrogen at 175°C, and completed dehydrogenation within 1 h at 275°C under the reported conditions. Interfacial charge redistribution and stabilization of nanoscale Mg/MgH_2 were associated with the improved sorption kinetics. The cryogenic adsorption and high-temperature hydride reactions, however, occur in widely separated operating regimes; their coexistence should not be interpreted automatically as a practically integrated wide-temperature storage function. Inorganic or reaction-derived scaffold phases can further combine confinement with interfacial catalysis. Ma et al. [90] confined MgH_2 crystallites of 5 to 10 nm within CoS nanoboxes derived from zeolitic imidazolate framework-67 (ZIF-67). During processing, an MgS-containing shell formed around MgH_2, providing catalytic interfaces and a physical barrier against particle coalescence (Figure 7b). An apparent dehydrogenation activation energy of 120.8 kJ mol^{-1} was reported. Changes in the measured reaction enthalpy were also observed, but establishing genuine thermodynamic destabilization requires reversible equilibrium measurements and consideration of possible additional reactions involving CoS and MgS. A complementary approach sought to overcome the low active-material loading common to porous scaffolds. Xing et al. [91] used in situ growth followed by thermal decomposition to confine approximately 8.7 nm Mg particles within a carbon framework at a reported Mg loading of 76.3 wt.% (Figure 7c). The combination of short transport distances and restricted particle growth reduced the apparent hydrogenation and dehydrogenation activation energies, while the carbon coating improved oxidation resistance and structural retention. The high Mg fraction is advantageous for gravimetric capacity, although volumetric packing density, pore accessibility, and retention of the nanoscale structure during extended cycling remain important evaluation criteria.

Overall, 3D scaffolds can integrate high active-material loading, particle stabilization, and distributed catalytic interfaces.

15214095, 0, Downloaded from https://advanced.onlinelibrary.wiley.com/doi/10.1002/adma.75618 by Cambridge University Library, Wiley Online Library on [05/11/2026]. See the Terms and Conditions (https://onlinelibrary.wiley.com/terms-and-conditions) on Wiley Online Library for rules of use; OA articles are governed by the applicable Creative Commons License

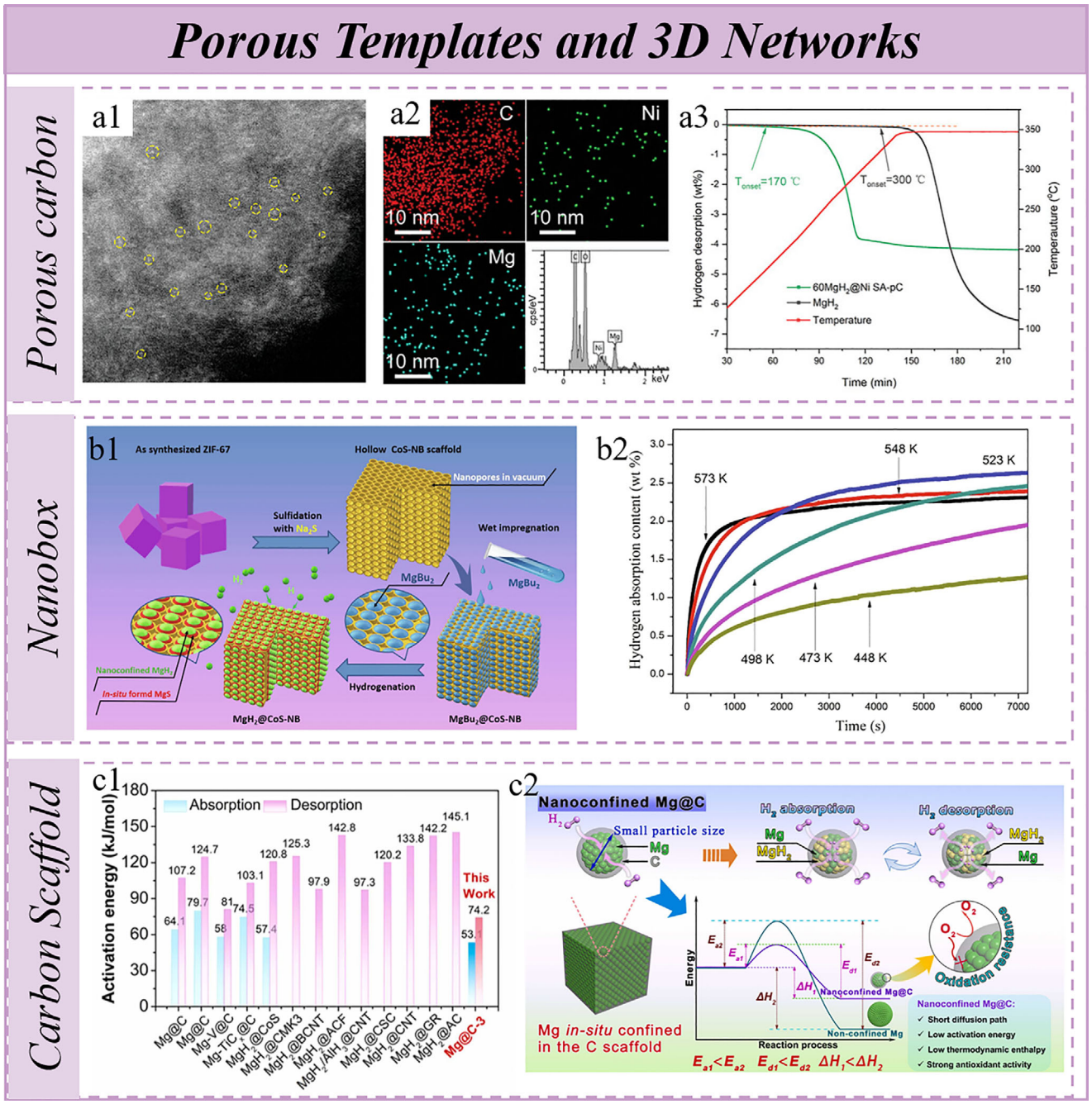


FIGURE 7 | Nanoconfinement of Mg-based hydrides using 3D porous scaffolds. (a1–a3) Representative microstructural images and thermal desorption behavior of MgH_2@Ni SA-pC. Adapted with permission [88]. Copyright 2025, Wiley. (b1, b2) Schematic preparation route and isothermal hydrogen absorption behavior of MgH_2@CoS-NBs. Adapted with permission [90]. Copyright 2021, Elsevier. (c1, c2) Comparative hydrogen storage performance and proposed dehydrogenation mechanism of Mg@C-3/MgH_2@C-3. Adapted with permission [91]. Copyright 2024, Elsevier.

Their advantages arise from the coupled effects of confinement, interface chemistry, and working-state phase evolution rather than from 3D geometry alone. Future comparisons should quantify MgH_2 loading, composite-level gravimetric and volumetric capacities, pore-filling efficiency, thermal conductivity, equilibrium thermodynamics, oxidation resistance, and long-term cycling. Although porous carbon can contribute additional cryogenic physisorption, this capacity is obtained under conditions distinct from those required for MgH_2 operation and should be reported separately when assessing system-level performance.

3.3 | Alloying Engineering

The high dehydrogenation enthalpy of MgH_2 reflects the free-energy difference between the MgH_2 and Mg + H_2 states and arises from the collective bonding and lattice energetics of the bulk phases rather than from a single Mg-H bond. Although bonding in MgH_2 has mixed ionic and covalent character, quantitative atomic charges depend on the partitioning method and should not be treated as unique oxidation states [92]. The calculated hydrogen adsorption energy at a stable site on the Mg

15214095, 0, Downloaded from https://advanced.onlinelibrary.wiley.com/doi/10.1002/adma.75618 by Cambridge University Library, Wiley Online Library on [05/11/2026]. See the Terms and Conditions (https://onlinelibrary.wiley.com/terms-and-conditions) on Wiley Online Library for rules of use; OA articles are governed by the applicable Creative Commons License

(11–20) surface is approximately −3.34 eV [93]. This value depends on the surface configuration and energy reference and should not be equated with the dehydrogenation enthalpy or activation energy of bulk MgH_2. Alloying introduces one or more elements into the Mg-based system to alter its phase stability, local coordination environment, electronic structure, and hydrogen reaction pathway [94]. Unlike conventional catalysts, which primarily accelerate the approach to equilibrium, alloying can modify equilibrium thermodynamics by stabilizing the dehydrogenated alloy, forming a ternary hydride with a different free energy, or enabling a multistep reaction pathway. Thermodynamic destabilization is not universal, however: its magnitude and direction depend on the relative free energies of all hydrogenated and dehydrogenated phases. Alloy formation may also reduce gravimetric capacity or introduce phase segregation and incomplete reversibility.

$$Mg_2Ni + 2H_2 \leftrightarrow Mg_2NiH_{0.3} + 1.85H_2 \leftrightarrow Mg_2NiH_4 \quad (6)$$

The Mg-Ni system provides a representative example, Mg_2NiH_4 [95]. Reilly and Wiswall showed that Mg_2Ni reacts reversibly with hydrogen, whereas $MgNi_2$ does not form a corresponding hydride under comparable conditions [96]. Mg_2Ni can form the ternary hydride Mg_2NiH_4, which has a theoretical gravimetric hydrogen capacity of approximately 3.6 wt.% and a dehydrogenation enthalpy of about +64.5 kJ mol^{-1} H_2, compared with approximately +75 kJ mol^{-1} H_2 for MgH_2 [97]. The lower reaction enthalpy increases the equilibrium hydrogen pressure at a given temperature, although this thermodynamic advantage is accompanied by a substantial reduction in hydrogen capacity. Hydrogenation initially produces a dilute interstitial solid solution, commonly represented as α- $Mg_2NiH_{0.3}$ (Equation 6), before transformation to Mg_2NiH_4 at higher hydrogen concentrations. The parent Mg_2Ni alloy has a hexagonal structure, whereas Mg_2NiH_4 exhibits temperature-dependent polymorphism: a monoclinic low-temperature phase and a higher-symmetry high-temperature phase [98, 99]. Formation of the hydride is accompanied by a large volume expansion of approximately 32%, which can promote particle fracture and loss of structural integrity during cycling. The bonding environment in Mg_2NiH_4 differs fundamentally from that in MgH_2 because hydrogen is coordinated primarily within complex $[NiH_4]^{4-}$ like units [100]. Its lower dehydrogenation enthalpy should therefore be attributed to the overall stability of the Mg_2Ni/Mg_2NiH_4 reaction couple rather than simply to weaker Mg—H bonds [101].

Zhang et al. [102] synthesized single-crystalline Mg_2NiH_4 nanoparticles by hydriding chemical vapor deposition and stabilized them on graphene using an approximately 3 nm MgO shell (Figure 8a). The shell suppressed particle coarsening during cycling while retaining short hydrogen-transport distances. Although MgO is commonly regarded as a kinetic barrier, this result shows that a sufficiently thin and structurally controlled oxide layer can instead function as a stabilizing shell; its effectiveness depends on maintaining adequate permeability to hydrogen. Interface engineering provides another route to accelerate hydrogen release without necessarily changing the intrinsic thermodynamics of Mg_2NiH_4. Zhao et al. [103] constructed a heterogeneous Mg-Ni material containing single-crystalline nanoscale Mg_2NiH_4 and $Mg_2NiH_4/MgNi_2$ interfaces (Figure 8b). Preferential dehydrogenation near these regions was proposed to generate local hydrogen-concentration gradients and accelerate transformation of the surrounding material. This behavior illustrates how spatially distributed phases with different reaction kinetics can initiate and propagate dehydrogenation, although direct evidence is required to distinguish concentration-gradient effects from interfacial catalysis and shortened diffusion lengths.

Substitution within the Mg_2Ni framework can more directly alter phase stability. Partial replacement of Ni by Cr or Mn in $Mg_2Ni_xM_{1-x}$ alloys (M = Cr or Mn) increased the equilibrium dehydrogenation pressure and lowered the reported hydride formation enthalpy [104]. These trends suggest that compositional substitution can destabilize the corresponding hydrogenated phases. The improvement is not necessarily monotonic or fully reversible, however, because elemental substitution may also promote phase segregation, reduce hydrogen capacity, or alter the reaction pathway. Equilibrium PCT measurements and phase-resolved cycling analyses are therefore required to establish the useful compositional range. Reaction-coupled alloys provide a distinct thermodynamic strategy. In the Mg-Si system, the reaction has a calculated dehydrogenation enthalpy of approximately 36.4 kJ mol^{-1} H_2, substantially lower than that of MgH_2 [105]. However, regeneration of Mg_2Si-derived materials by direct hydrogenation is kinetically difficult, limiting practical reversibility [106]. Trace Na addition to a hypoeutectic Mg-1 wt.% Si alloy increased its hydrogen uptake from 0.31 to 6.72 wt.% at 350°C and 2 MPa H_2 (Figure 8c) [107]. Na modified the surface oxide layer, forming porous Na_2O and NaOH that facilitated hydrogen permeation. In situ diffraction showed that Mg_2Si remained stable during hydrogen sorption. This example illustrates how surface chemistry can govern the accessible hydrogen capacity of a Mg-rich alloy under the reported conditions. Related alloy systems display different balances between capacity and thermodynamic stability. Mg_2Cu reacts with hydrogen through disproportionation to form MgH_2 and $MgCu_2$ rather than a stable Mg_2Cu hydride [108]. By contrast, Mg_2CoH_5 is a ternary complex hydride with a theoretical hydrogen capacity of approximately 4.5 wt.% and a dehydrogenation enthalpy of about 82.3 kJ mo^{l-1} H_2 [109]. Its stronger thermodynamic stability illustrates that alloying does not inherently lower the reaction enthalpy. Rare-earth-containing Mg alloys likewise often undergo disproportionation during the first hydrogenation, generating rare-earth hydrides that subsequently act as persistent catalytic or hydrogen-transfer phases rather than remaining as homogeneous Mg alloys. Complex hydrides can also function as dynamically generated catalyst precursors. Mg_2FeH_6, synthesized from Mg and Fe despite their limited mutual solubility, has a volumetric hydrogen capacity of approximately 150 kg H_2 m^{-3} [110]. Its formation enthalpy of approximately −77.4 kJ mol^{-1} H_2 indicates slightly greater thermodynamic stability than MgH_2 and therefore does not provide intrinsic destabilization [111]. Using in situ transmission electron microscopy, Kim et al. observed the decomposition of Mg_2FeH_6 into Mg-containing products and nanoscale Fe clusters within an Mg_2FeH_6-MgH_2 composite (Figure 8d) [112]. The reaction-derived Fe clusters accelerated subsequent MgH_2 dehydrogenation, demonstrating that a comparatively stable complex hydride can improve composite kinetics through dynamic catalyst generation even when it does not lower the equilibrium reaction enthalpy.

Collectively, Mg alloying operates through several distinct mechanisms: stabilization of a dehydrogenated intermetallic phase,

15214095, 0, Downloaded from https://advanced.onlinelibrary.wiley.com/doi/10.1002/adma.75618 by Cambridge University Library, Wiley Online Library on [05/11/2026]. See the Terms and Conditions (https://onlinelibrary.wiley.com/terms-and-conditions) on Wiley Online Library for rules of use; OA articles are governed by the applicable Creative Commons License

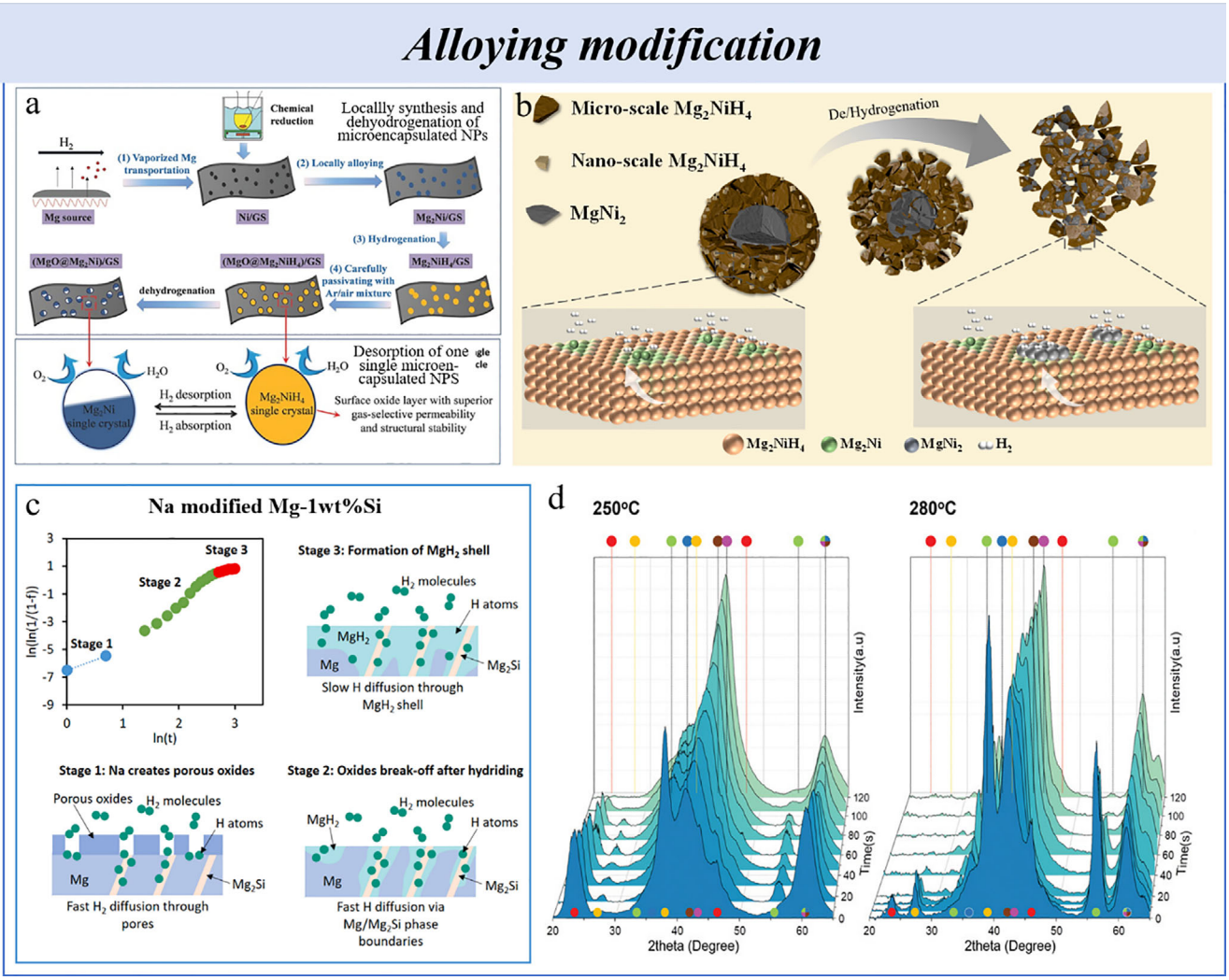


FIGURE 8 | Alloying strategies for modifying Mg-based hydrogen storage materials. (a) Preparation of microencapsulated ultrafine Mg_2NiH_4 nanoparticles and their structural evolution during hydrogen cycling. Adapted with permission [102]. Copyright 2017, Wiley. (b) Proposed hydrogen storage mechanism in structurally heterogeneous Mg-Ni composite hydrides. Adapted with permission [103]. Copyright 2023, The Royal Society of Chemistry. (c) Hydrogen storage processes in unmodified and Na-modified Mg-1 wt.% Si alloys. Adapted with permission [107]. Copyright 2022, Elsevier. (d) Waterfall plots showing the dehydrogenation evolution of Mg_2FeH_6-MgH_2 composites. Adapted with permission [112]. Copyright 2022, Wiley.

formation of a ternary hydride, compositional substitution, disproportionation, and generation of catalytic phases during cycling. These mechanisms must not be grouped under the assumption that alloying universally destabilizes MgH_2. Meaningful comparisons should consider equilibrium pressure, reaction enthalpy, reversible composite-level capacity, phase reversibility, volume change, catalyst evolution, and long-term structural stability.

3.4 | External Field Assistance

Although catalysis, nanostructuring, and alloying can accelerate hydrogen sorption or modify reaction thermodynamics, most Mg-based hydrides still require substantial heat input to achieve practically relevant rates. External energy fields, particularly light [113] and microwaves [114], offer alternative routes for delivering this energy. Their potential advantage lies in rapid, spatially selective, or volumetric energy deposition rather than an inherent reduction in the heat required by the Mg/MgH_2 reaction. Field-assisted operation may also alter interfacial charge distributions or generate reactive carriers, but such nonthermal contributions must be separated from local heating through appropriate temperature measurements and control experiments [115]. Whether these approaches reduce system-level energy consumption ultimately depends on field-to-heat conversion efficiency, penetration depth, heat loss, reactor geometry, and the energy required to generate the applied field.

Light-assisted hydrogen sorption can proceed through photothermal and, potentially, photochemical pathways [116, 117]. In the photothermal pathway, absorbed photons are converted into heat near an optically active component, producing local temperatures that may exceed the measured average temperature of the sample. Photochemical pathways instead involve direct participation of photoexcited electrons or holes in interfacial reactions. Early ultraviolet-irradiation experiments on alkaline-earth hydrides demonstrated that light can induce hydride decomposition

15214095, 0, Downloaded from https://advanced.onlinelibrary.wiley.com/doi/10.1002/adma.75618 by Cambridge University Library, Wiley Online Library on [05/11/2026]. See the Terms and Conditions (https://onlinelibrary.wiley.com/terms-and-conditions) on Wiley Online Library for rules of use; OA articles are governed by the applicable Creative Commons License

and suggested that photoexcited carriers may contribute before a continuous product-reactant interface develops [118]. However, distinguishing direct photochemical decomposition from irradiation-induced heating remains experimentally challenging. Plasmonic metals provide a means of concentrating optical energy near Mg-based particles. Sun et al. [119] incorporated Au nanoparticles into Mg and reported hydrogen uptake under illumination at a measured bulk temperature of approximately 100°C. The effect was attributed to localized surface plasmon resonance and the resulting nanoscale thermal gradients. The responsive region extended only several nanometers around the Au particles, illustrating both the kinetic potential and the spatial limitation of localized photothermal heating. Such measurements demonstrate that the local reaction environment can differ substantially from the macroscopic temperature, but they do not alone establish a reduction in equilibrium hydrogenation temperature or total energy demand. More recent designs combine broadband light absorption with catalytic hydrogen exchange. The Cu@MXene catalyst coupled the plasmonic response of Cu nanoparticles with light absorption by the MXene support [120]. Ti- and TiH_x-containing phases generated during processing were proposed to facilitate H_2 dissociation, recombination, and interfacial hydrogen transfer. It reported the first demonstration of solar-driven reversible hydrogen storage in an Mg-based solid-state hydrogen storage material. The composite retained a reversible capacity of 5.9 wt.% after 30 light-assisted cycles, indicating that the coupled photothermal and catalytic functions remained effective over the reported cycling period. An alternative strategy is to incorporate optical absorption directly into the hydrogen storage phase. Atomic reconstruction of Mg_2Ni(Cu)-based materials produced broadband absorption exceeding 85% over 250–2000 nm, which was associated with an electronic structure favorable for photon absorption and photothermal conversion (Figure 9a) [121]. This integration reduces reliance on a separate photothermal additive, but optical absorptance alone does not determine hydrogen-storage efficiency. Thermal conductivity, radiative and convective losses, catalyst stability, and the fraction of absorbed energy delivered to the hydride reaction must also be quantified. Evidence from in situ X-ray photoelectron spectroscopy (XPS), femtosecond transient absorption spectroscopy (fs-TAS) measurements, and theoretical calculations support photoinduced carrier trapping and interfacial charge transfer in MgH_2/STO-450 (Figure 9b) [122]. These findings suggest that photogenerated carriers may contribute to the improved sorption kinetics alongside photothermal heating. Across the studies reviewed, photothermal conversion can deliver heat near reactive regions and accelerate MgH_2 desorption, whereas hydrogen absorption still requires pressure and temperature conditions favorable for the hydride formation. Ti/TiH_x-containing interfaces have been proposed to facilitate H_2 dissociation, recombination, and interfacial hydrogen transport. Mg_2Ni(Cu)-based phases combine broadband light absorption with alloy and hydride chemistry that alters their reaction pathways and energetics. These effects arise from the material composition and working phases rather than illumination-induced destabilization of MgH_2. The available evidence therefore supports complementary contributions from local heating, catalytic interfaces, and, in some systems, photoinduced carriers. Their relative importance remains dependent on the material and operating conditions. Quantifying the carrier contribution requires operando measurements of carrier dynamics and interfacial chemical states, together with dark controls conducted at matched local temperatures. Light-assisted designs have progressed from added plasmonic absorbers to multifunctional interfaces and intrinsically light-absorbing storage phases. Practical translation will require effective illumination of optically thick beds, durable components, reliable internal-temperature measurements, heat management, and energy balances benchmarked against conventional heating.

Microwave irradiation can heat hydrogen storage materials through dielectric, conductive, and, where relevant, magnetic losses. In contrast to surface heating followed by thermal conduction, microwaves may deposit energy throughout part of the reaction bed, potentially enabling rapid volumetric heating. This advantage is not universal, however, because penetration depth and heating uniformity depend on frequency, field distribution, reactor geometry, temperature-dependent electromagnetic properties, and the dimensions of the bed. Microwave heating should therefore not be assumed to be more energy-efficient than resistive heating without a system-level comparison based on the same thermal and reaction boundaries. Early studies by Nakamori et al. examined the microwave response of metal and complex hydrides and showed that heating behavior varies strongly with dielectric properties and phase composition [123, 124]. Because MgH_2 itself may couple only weakly or non-uniformly with microwave fields, microwave-responsive additives such as carbonaceous materials and transition-metal compounds have been introduced as susceptors [125, 126]. These phases absorb electromagnetic energy and transfer the resulting heat to the surrounding hydride, but they may also produce local temperature gradients that are difficult to capture using external temperature measurements.

The reported change in Ti oxidation state and enhanced hydrogen sorption suggest that microwave irradiation may affect catalyst evolution beyond providing a heat source [127]. As with light-assisted sorption, however, a field-specific contribution must be distinguished from localized heating. This could be tested by comparing microwave irradiation with conventional heating under the same hydrogen pressure and closely matched measured temperature-time profiles. Microwave-compatible multipoint thermometry, combined with operando measurements of Ti oxidation state, phase evolution, and hydrogen-release rate, would establish a thermal baseline for this comparison. Field-on and field-off tests at controlled temperature could provide a further check. A difference beyond measurement uncertainty would support a microwave-specific contribution, although unresolved nanoscale hot spots would still need to be considered. At the reactor scale, Wang et al. combined a graphite susceptor with a $NaTiO_xH$-modified MgH_2 bed and developed a multiphysics model coupling microwave propagation, heat transfer, mass transport, and hydride decomposition (Figure 9c) [128]. Under the modelled conditions, graphite-assisted microwave heating improved bed-temperature uniformity, reduced dehydrogenation time by 53.49%, and lowered energy consumption by at least 10.71% relative to the selected electric-heating configuration. Increasing microwave power shortened the simulated reaction time, with reductions of up to 19.55% for each 20 W increment over the investigated range. This effect reflects faster energy delivery and reaction kinetics rather than an improvement in dehydrogenation thermodynamics. The model further identified 2.1 GHz and 2 wt.% graphite as favorable parameters for the

15214095, 0, Downloaded from https://advanced.onlinelibrary.wiley.com/doi/10.1002/adma.75618 by Cambridge University Library, Wiley Online Library on [05/11/2026]. See the Terms and Conditions (https://onlinelibrary.wiley.com/terms-and-conditions) on Wiley Online Library for rules of use; OA articles are governed by the applicable Creative Commons License

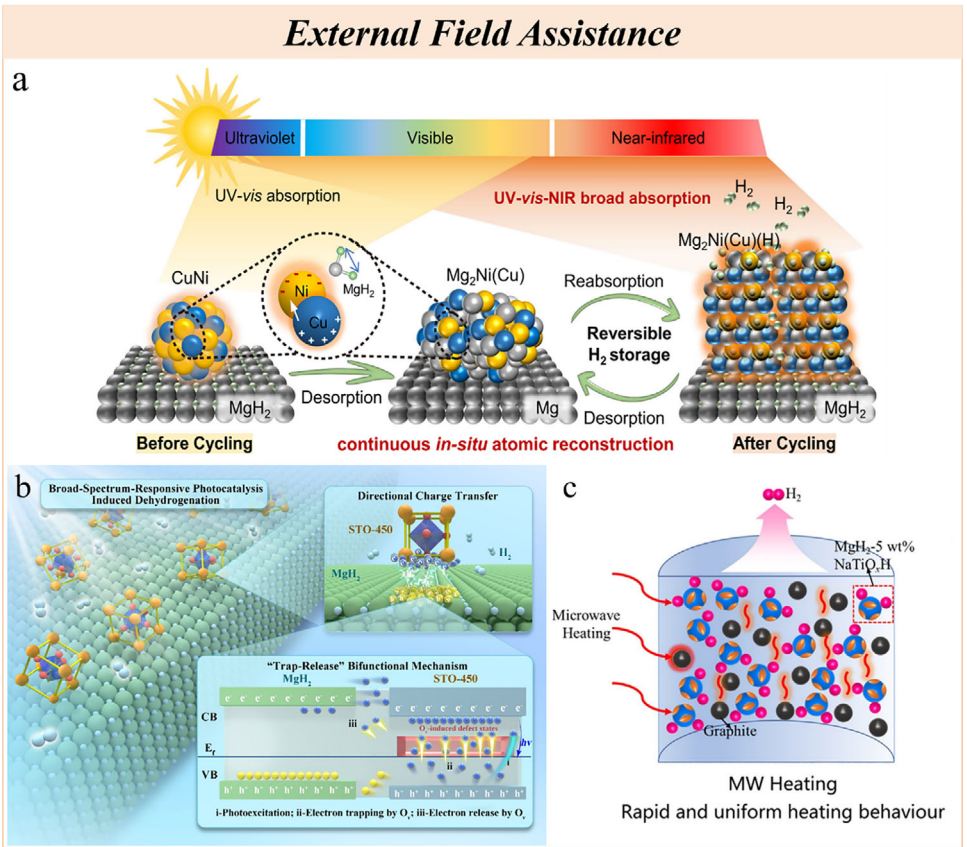


FIGURE 9 | External field-assisted hydrogen storage in Mg-based materials. (a) Proposed mechanism for the combined photothermal and catalytic enhancement of hydrogen storage in $Mg_2Ni(Cu)/Mg_2Ni(Cu)(H)$. Adapted under the terms of the Creative Commons Attribution 4.0 International License [121]. The Author(s) 2024. (b) Proposed photothermally assisted photocatalytic dehydrogenation mechanism at the MgH_2/STO-450 heterointerface. Adapted with permission [122]. Copyright 2025, Wiley. (c) Microwave-assisted MgH_2-$NaTiO_xH$ hydrogen storage reactor and the corresponding multiphysics model. Adapted with permission [128]. 2025 Chongqing University.

specific reactor geometry and material properties considered; these values should not be regarded as universal optima.

Overall, microwave-assisted hydrogen release offers potential advantages in heating rate, spatial energy deposition, and integration of microwave-responsive catalysts with reactor thermal management. Its practical benefit must nevertheless be evaluated using experimentally validated electromagnetic and thermal properties, spatially resolved temperature measurements, generator and coupling losses, hydrogen productivity, and total specific energy consumption.

External-field-assisted strategies, particularly optical and microwave excitation, provide alternative means of controlling the spatial and temporal delivery of energy to Mg-based hydrogen storage materials. Research has progressed from demonstrating field-responsive hydrogen sorption to designing multifunctional systems that integrate energy absorption, local heat generation, interfacial catalysis, and hydrogen transport. Proposed mechanisms extend beyond photothermal or microwave heating to include carrier-mediated interfacial reactions and field-induced changes in catalyst oxidation state. However, these nonthermal contributions remain difficult to distinguish from localized temperature gradients and require matched-temperature controls, operando characterization, and spatially resolved thermal measurements. Future research should prioritize quantitative relationships among field absorption, local temperature, catalyst evolution, and hydrogen reaction rates. Although coupling optical, thermal, electrical, or microwave stimuli may provide additional control over energy deposition, added complexity is justified only if it improves hydrogen productivity or system efficiency. Practical evaluation must therefore extend beyond reductions in onset temperature or reaction time to include field-generation and coupling losses, penetration depth, temperature uniformity, specific energy consumption, reversible capacity, cycling durability, and reactor scalability. Establishing these metrics will determine whether field-assisted concepts offer genuine advantages over optimized conventional heating.

4 | Data-Driven Discovery of Mg-Based Hydrogen Storage Materials

Catalysis, nanoconfinement, alloying, and external field assistance have generated increasing amounts of data on Mg-based hydrogen storage materials. These data connect composition, synthesis, structure, and testing conditions with thermodynamic and kinetic performance. Machine learning can identify relationships within these multidimensional datasets and prioritize

15214095, 0, Downloaded from https://advanced.onlinelibrary.wiley.com/doi/10.1002/adma.75618 by Cambridge University Library, Wiley Online Library on [05/11/2026]. See the Terms and Conditions (https://onlinelibrary.wiley.com/terms-and-conditions) on Wiley Online Library for rules of use; OA articles are governed by the applicable Creative Commons License

candidates for experimental validation. Potential applications include catalyst screening, scaffold optimization, alloy design, property prediction, and descriptor discovery. Model-derived correlations must nevertheless be validated through experiments or physics-based calculations. Machine learning should therefore complement physical understanding and targeted experimentation. A useful workflow uses model predictions to select experiments, incorporates the resulting data into subsequent training, and applies mechanistic analysis to constrain future predictions. This iterative process requires standardized data, complete experimental metadata, uncertainty estimates, and prospective validation using materials outside the training set. This section examines representations and learning methods suited to the limited and heterogeneous data available for Mg-based hydrides. It then evaluates their application to property prediction and descriptor discovery.

4.1 | Reliable Machine Learning for Mg-Based Hydrides

Reliable machine learning depends on data quality, material representation, algorithm selection, and validation [129]. For Mg-based hydrides, model inputs should describe not only composition and crystal structure, but also particle size, catalyst loading, defect density, surface state, and synthesis history. Experimental conditions are equally important. Temperature, hydrogen pressure, heating rate, conversion fraction, and capacity basis should be recorded alongside each target value. Pooling studies with incompatible labels or missing metadata can make a model learn testing protocols rather than material behaviors. Physically meaningful descriptors are particularly valuable for the small datasets available in this field. Relevant examples include hydride formation energy, metal-to-hydrogen bonding indicators, hydrogen transport distance, catalyst electronic properties, and interfacial characteristics. More flexible representations can capture complex local environments, but they generally require larger and more consistent datasets. The center and environment framework proposed by Xiao et al. [130] illustrates how local chemistry and extended structural information can be combined under limited data conditions. Experimental characterization can provide additional descriptors, although instrumental differences and data processing may introduce systematic bias.

Model complexity should match the scale and quality of the data [131]. Regularized regression, tree-based ensembles, kernel methods, and Gaussian processes are often suitable for limited datasets. More complex neural networks can represent nonlinear relationships, but their extrapolation remains uncertain with sparse and heterogeneous data. Graph-derived features and symbolic regression have been combined in broader materials models [132]. Bayesian inference has also been used to extract x-ray diffraction peak features for machine learning in another material system [133]. Validation should reflect the intended prediction task. Tests that hold out entire publication sources or composition families probe transfer to independent studies and new material classes more directly than random splits. Reported errors should be accompanied by calibrated prediction uncertainty and a stated range of applicable compositions and operating conditions. Candidates outside that range can guide targeted data collection, while their predicted performance still requires independent testing. Bayesian optimization can guide sequential experiments by balancing model uncertainty with predicted performance. Its objective should include reversible capacity, equilibrium pressure, sorption rate, cycling stability, cost, and operating conditions. Optimizing onset temperature alone may favor materials with high additive contents or poor practical capacity. Large language models may support literature mining and dataset construction, but all extracted values require traceable sources and expert verification. Machine-learned interatomic potentials provide a complementary route for accelerating atomistic simulations. They approximate potential energy surfaces using first principles training data and enable molecular dynamics over larger spatial and temporal scales than direct ab initio methods. Batatia et al. [134] developed a general-purpose atomistic foundation model based on the Message Passing Atomic Cluster Expansion framework. The model combines equivariant message passing with atomic cluster representations to predict energies, forces, and stresses across diverse chemical environments. The model can be fine-tuned using data from a target system, while this general-purpose study does not validate its predictions for MgH_2 or MgH_2/catalyst interfaces.

Studies directly related to Mg-based systems have addressed more specific problems. Angeletti et al. [135] compared pretrained and fine-tuned machine-learned potentials for hydrogen diffusion in metallic Mg and showed the importance of representative hydrogen-defect configurations. Wang et al. [136] separately trained a Deep Potential for the Mg-H system and applied it to hydrogen diffusion in two MgH_2 polymorphs. Modeling MgH_2/catalyst interfaces requires training or fine-tuning data that cover the relevant compositions, defects, interfacial structures, and reaction configurations. Predictions should then be validated against first-principles calculations and, where possible, experiments.

4.2 | Performance Prediction and Descriptor Discovery

Machine learning research on Mg-based hydrides follows two closely related directions. The first predicts hydrogen storage properties to support material screening. The second identifies physically meaningful descriptors that connect composition and structure with thermodynamic or kinetic performance.

4.2.1 | Predictive Models for Hydrogenation/Dehydrogenation Properties

Supervised learning is currently the most widely used approach for predicting hydrogen storage capacity, reaction enthalpy, desorption temperature, and kinetic parameters. Random forests, support vector regression, and gradient boosting methods can capture nonlinear relationships using relatively small datasets [137]. Their predictive value is nevertheless limited by inconsistent experimental conditions and incomplete metadata. In particular, onset temperature and apparent activation energy depend on the measurement protocol and kinetic model. Including testing conditions as model inputs can improve prediction and comparability, but onset temperature

15214095, 0, Downloaded from https://advanced.onlinelibrary.wiley.com/doi/10.1002/adma.75618 by Cambridge University Library, Wiley Online Library on [05/11/2026]. See the Terms and Conditions (https://onlinelibrary.wiley.com/terms-and-conditions) on Wiley Online Library for rules of use; OA articles are governed by the applicable Creative Commons License

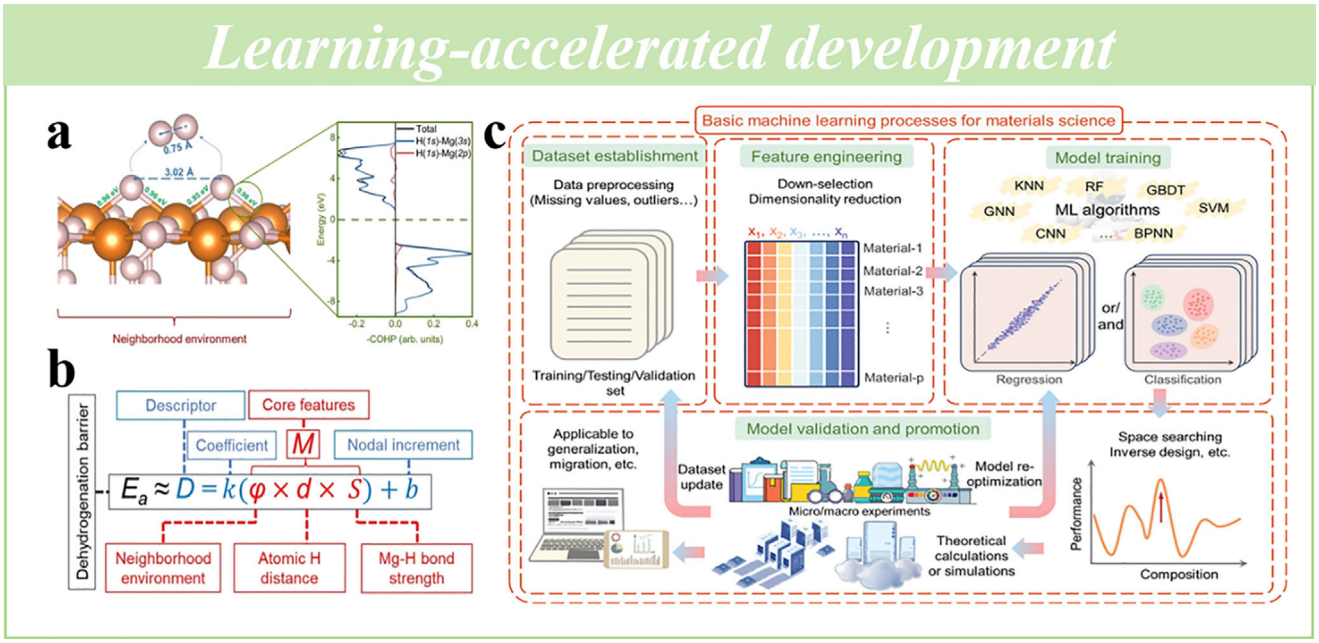


FIGURE 10 | Machine-learning-assisted investigation of Mg-based hydrides. (a, b) Construction of physically informed descriptors for predicting MgH_2 dehydrogenation kinetics. Adapted with permission [139]. Copyright 2024, Wiley. (c) General machine learning workflow for materials research. Adapted with permission [140]. Copyright 2025, Wiley.

and apparent activation energy remain protocol-dependent quantities rather than intrinsic material constants.

Gaussian process regression is well suited to sparse datasets because it provides predictions together with uncertainty estimates. When coupled with active learning, it can prioritize calculations expected to provide the most useful information. Lin et al. [138] developed a physics-informed Gaussian process regression framework for predicting the adsorption energies of intermediates in methylcyclohexane dehydrogenation and used an active-learning workflow to examine the data-efficient model construction. The models used fewer than 100 data points for each reaction intermediate and achieved test-set mean absolute errors of 0.11–0.25 eV. Although this study concerned a liquid organic hydrogen carrier rather than MgH_2, it illustrates a data-efficient strategy for selecting informative calculations in chemically complex catalytic systems. Its application to Mg-based hydrides will require Mg-specific descriptors, representative training data, and independent validation.

Physics-informed feature construction provides another route to reducing data requirements. Li et al. [139] developed a model for the dehydrogenation barrier of MgH_2 using indicators derived from crystal orbital Hamilton population analysis and hydrogen separation distances (Figure 10a,b). These quantities were combined into a distance-energy ratio that represents contributions from Mg to hydrogen bond weakening and hydrogen recombination. The study shows that a simple model can remain predictive and interpretable when its inputs reflect the underlying reaction physics. However, the transferability of the descriptor across different catalysts, interfaces, particle sizes, and reaction pathways must be established using independent data.

A central challenge is balancing predictive performance with physical interpretability [140]. Complex models may achieve low errors within cross validation but fail when applied to new chemical families. Interpretable models are easier to relate to reaction mechanisms, but their performance depends strongly on whether the selected descriptors remain valid outside the training domain (Figure 10c). This limitation is important for Mg-based hydrides because thermodynamics, surface reactions, nucleation, and hydrogen transport contribute simultaneously to measured performance [141].

4.2.2 | Descriptors Governing Mg Hydride Performance

The thermodynamics and kinetics of Mg-based hydrides are governed by Mg to hydrogen bonding, hydrogen recombination, phase nucleation, and transport through the evolving Mg and MgH_2 phases. Identifying descriptors that represent these processes is essential for developing transferable predictive models. Early calculations linked lower dehydrogenation barriers to longer Mg to hydrogen bonds and reduced bond order [141]. However, individual structural descriptors often fail across catalyzed, alloyed, or nanoconfined systems because they do not capture changes in electronic structure and reaction pathway.

Li et al. [139] combined the integrated crystal orbital Hamilton population of the Mg to hydrogen bond with the nearest hydrogen to hydrogen distance to construct a distance-to-energy ratio. The integrated crystal orbital Hamilton population describes bond strength, while the hydrogen separation reflects the geometric requirement for molecular hydrogen formation. Their combination therefore represents two coupled steps in dehydrogenation, namely Mg to hydrogen bond cleavage and hydrogen

15214095, 0, Downloaded from https://advanced.onlinelibrary.wiley.com/doi/10.1002/adma.75618 by Cambridge University Library, Wiley Online Library on [05/11/2026]. See the Terms and Conditions (https://onlinelibrary.wiley.com/terms-and-conditions) on Wiley Online Library for rules of use; OA articles are governed by the applicable Creative Commons License

recombination. The resulting model predicted energy barriers across several modified MgH_2 systems. Its transferability should nevertheless be tested using independent material classes and interface structures. Descriptors for catalytic and interfacial effects remain less established. Potential variables include the d band center of a transition metal catalyst, interfacial metal-to-hydrogen bond strength, charge transfer, hydrogen adsorption energy, and hydrogen migration barriers [142]. Their predictive value may depend on catalyst oxidation state, coordination environment, and structural evolution during cycling. Descriptors derived from the initial catalyst structure may therefore fail to represent the active phase under operating conditions.

Future descriptor development should integrate electronic, structural, interfacial, and transport variables that represent catalysts under operating conditions. Their value should be assessed by their physical meaning and transferability across different Mg-based material classes.

5 | System Integration, Application, and Techno-Economic Analysis

Machine learning is being explored for thermal management in solid-state hydrogen storage systems. At reactor scale, effective bed thermal conductivity, gas permeability, and reaction enthalpy govern transient temperature and hydrogen-pressure fields [143, 144]. The internal heat exchangers improve thermal control while adding mass and occupy volume otherwise available for hydrides. Bed expansion and contraction can change interparticle contact, thermal resistance, and hydrogen flow paths during cycling. Such changes may produce nonuniform hydrogen distribution and reduce durability. The thermal mass of the bed and vessel also influences start-up time and the initial hydrogen delivery rate. These coupled effects determine whether improved powder-level kinetics are retained in a reactor. Numerical models are widely used to analyze these coupled processes. Early models, such as those by El Osery [145], Lucas [146], Jemni [147], and Mat [148], established descriptions of heat and mass transfer in metal hydride beds. Recent studies have extended these approaches to reactor geometries and operating conditions relevant to larger systems. Lin et al. [149] developed a coupled model that represented 1D heat transfer fluid flow and 3D reactions within a multiton Mg-Ni storage bed (Figure 11a). Comparison with experimental data allowed the effects of fluid temperature and flow rate to be assessed while limiting computational cost. Shao et al. [150] examined a direct hydrogen heating configuration that used hot hydrogen as both the reactant and the heat transfer medium (Figure 11b). This design removed the internal heat exchanger and increased the available volume for storage material. The model indicated that inlet temperature and bed geometry strongly affected reaction uniformity. Vacuum assistance during the initial desorption stage was also predicted to suppress local rehydrogenation. However, the associated pumping energy and system complexity must be included when assessing the net benefit. Direct hydrogen heating may be most relevant when high-temperature hydrogen or waste heat is already available from coupled equipment. Engineering demonstrations provide initial evidence of scale up. A prototype containing approximately 1200 kg of Mg-Ni hydride reportedly stored and released 75.3 kg of hydrogen within 12 h, with a volumetric hydrogen density of 54.3 kg m^{-3} (Figure 11c) [151]. A subsequent 40 foot transport unit contained approximately 14.4 t of storage material and carried more than 860 kg of hydrogen (Figure 11d). A second generation 20 foot unit reportedly increased the hydrogen capacity to about 1005 kg (Figure 11e). Related systems have also been demonstrated at hydrogen refueling facilities (Figure 11f). These results indicate that Mg-based systems can achieve high hydrogen capacity per unit container volume under relatively low hydrogen pressure. Comparisons with compressed gas trailers must nevertheless use consistent boundaries. Vessel mass, heat exchange equipment, auxiliary components, usable hydrogen fraction, charging time, delivery pressure, and energy consumption should all be included. LLong-termfield data are also required to establish cycling durability, thermal performance, maintenance requirements, and operational safety.

A cross-technology sustainability assessment highlights the need to consider cost, energy use, and environmental impacts together [152]. Application-specific techno-economic analysis is needed to compare Mg-based storage with compressed hydrogen, liquid hydrogen, and other carriers. Material advances create system value through usable hydrogen inventory, throughput, heat demand, and component lifetime. Indeed, higher reversible hydrogen storage capacity of the composite can reduce the required hydride inventory and vessel size. Catalyst loading, catalyst price, and synthesis complexity affect material and fabrication costs. Faster sorption kinetics can increase delivery rate when reactor heat and gas transfer sustain the same throughput. Lowering the temperature needed for a specified rate can improve compatibility with available process heat, when the equilibrium pressure remains adequate. Wang et al. [153] analyzed photovoltaic-powered solid oxide electrolysis coupled with Mg-based storage and transport, including recovery of magnesium hydrogenation heat. Their scenario analysis linked economic outcomes to electricity price, heat integration, material lifetime, and transport distance. These variables should be put into application-specific mass and energy balances and evaluated as usable system capacity and cost per kilogram of hydrogen delivered.

Stationary buffers for hydrogen produced from intermittent renewable electricity can exploit compact, low-pressure storage when charging and discharging are scheduled. Industrial sites offer a further opportunity where waste heat can support hydrogen release at a compatible temperature. Conversely, heat released during hydrogenation can be recovered for a coupled high-temperature process, as explored in the electrolysis-based pathway. The reversible de/hydrogenation reactions also support the thermochemical heat storage, a distinct service with its own heat and hydrogen balance. Containerized transport and refueling supply have reached initial engineering demonstration, but require suitable turnaround time, heating infrastructure, and delivery pressure. Each application should be assessed using usable capacity, response time, full-cycle energy use, and delivered hydrogen cost under a defined duty cycle.

6 | Outlook and Conclusion

Mg-based hydrogen storage combines high material-level capacity, resource abundance, and operation at relatively low hydrogen

15214095, 0, Downloaded from https://advanced.onlinelibrary.wiley.com/doi/10.1002/adma.75618 by Cambridge University Library, Wiley Online Library on [05/11/2026]. See the Terms and Conditions (https://onlinelibrary.wiley.com/terms-and-conditions) on Wiley Online Library for rules of use; OA articles are governed by the applicable Creative Commons License

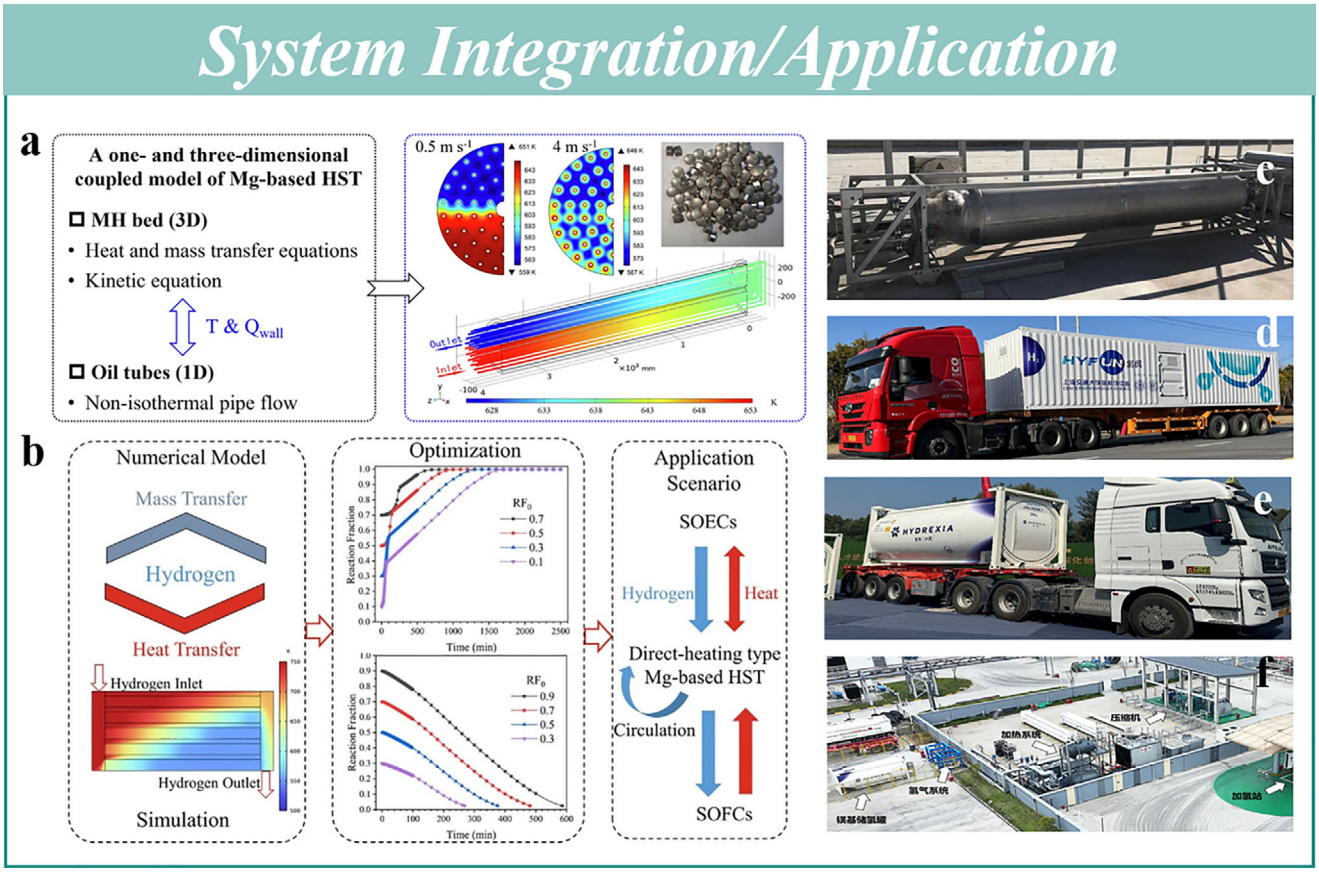


FIGURE 11 | System integration and engineering applications of Mg-based solid-state hydrogen storage. (a) Coupled 1D and 3D model of a Mg-based hydrogen storage tank and its experimental validation. Adapted with permission [149]. Copyright 2023, Elsevier. (b) Direct hydrogen-heated Mg-based solid-state hydrogen storage system and its control strategy for regulating hydrogen absorption and desorption. Adapted with permission [150]. Copyright 2024, Elsevier. (c) Large-scale oil-heated Mg-based hydrogen storage system. (d) First-generation tonne-scale Mg-based solid-state hydrogen storage and transportation trailer. (e) Second-generation tonne-scale Mg-based solid-state hydrogen storage and transportation trailer. (f) Demonstration of the second-generation tonne-scale Mg-based hydrogen storage system at a hydrogen refueling station. Adapted with permission [151]. Copyright 2025, Elsevier.

pressure. Its practical performance, however, is governed by coupled constraints across several length scales. Equilibrium thermodynamics defines the accessible pressure and temperature range. Surface reactions, nucleation, and hydrogen transport control the intrinsic sorption rate. Heat and mass transfer then determine whether this performance can be retained in a reactor. No single modification strategy resolves all of these constraints.

Across the studies reviewed, improvements in Mg-based hydrogen storage are associated with coordinated changes in composition, microstructure, and the interfaces present during cycling. Catalytic phases and nanostructures can work together to promote H_2 dissociation and recombination, shorten hydrogen diffusion paths, and facilitate Mg/MgH_2 nucleation. Electronic interactions at these interfaces may modify local hydrogen binding and reaction barriers. Alloying can alter the relative stability of hydrogenated and dehydrogenated phases while creating intermetallic interfaces that accelerate hydrogen sorption. At sufficiently small dimensions, surface and interfacial energies may also influence hydride equilibrium. Light or microwave assistance provides additional control over energy delivery, yet their reactor-level value depends on conversion efficiency and heat management. The choice of strategies should reflect the intended operating conditions. Their benefits should be assessed in terms of reversible composite capacity, sorption rates, cycling durability, processing complexity, catalyst cost, and overall energy demand.

6.1 | Enable Transparent and Context Aware Benchmarking

Hydrogen storage performance depends on both material properties and measurement conditions. Onset temperature, apparent activation energy, reversible capacity, and cycling stability should therefore be interpreted together with the experimental protocol used to obtain them. Future studies should report essential metadata, including additive fraction, composite level capacity, sample mass, hydrogen pressure, heating rate, kinetic model, conversion range, and activation procedure. Identical testing conditions across all studies are neither practical nor necessary. Instead, comparisons should be restricted to sufficiently similar conditions or supported by appropriate normalization and uncertainty analysis. A lower desorption onset is a useful measure of hydrogen-release performance under the

15214095, 0, Downloaded from https://advanced.onlinelibrary.wiley.com/doi/10.1002/adma.75618 by Cambridge University Library, Wiley Online Library on [05/11/2026]. See the Terms and Conditions (https://onlinelibrary.wiley.com/terms-and-conditions) on Wiley Online Library for rules of use; OA articles are governed by the applicable Creative Commons License

reported protocol. By itself, it does not establish a change in equilibrium thermodynamics, which should be evaluated independently using PCT measurements under well-defined conditions.

6.2 | Resolve Working State Mechanisms and Long-Term Degradation

Many active catalysts form only during milling or hydrogen cycling. Their initial structures may differ substantially from the phases that control hydrogen exchange. Operando diffraction, spectroscopy, microscopy, and isotope tracing should be combined with first-principles calculations and machine-learned interatomic potentials. These methods can identify active interfaces, hydrogen transport pathways, and rate-controlling steps. Equal attention should be given to particle coarsening, oxidation, phase segregation, volume change, and loss of interfacial contact. Mechanistic understanding is useful only if it explains both initial activity and performance retention.

6.3 | Design Materials for Reactor Requirements

Material optimization should begin with the operating conditions of the intended application. Relevant targets include delivery pressure, hydrogen flow rate, available heat source, charging time, packing density, and cycle life. High powder capacity does not guarantee high system capacity because scaffolds, catalysts, heat exchangers, vessels, and auxiliary equipment add mass and volume. The effective thermal conductivity and mechanical evolution of the packed bed should be treated as material design variables. Co-design of the storage material, bed architecture, heat exchanger, and control strategy is therefore essential.

6.4 | Connect Data Driven Discovery With Deployment Boundaries

Machine learning can support catalyst screening, descriptor discovery, and experimental selection. Its value depends on standardized data, complete metadata, calibrated uncertainty, and validation on unseen material classes. Models should optimize multiple objectives rather than onset temperature alone. These objectives should include reversible capacity, equilibrium pressure, kinetics, stability, cost, and synthesis feasibility. Techno-economic and life cycle assessments should use consistent system boundaries when comparing Mg-based storage with compressed hydrogen, liquid hydrogen, and other carriers. Transport distance, heat availability, delivery pressure, electricity cost, material lifetime, and recycling should be included.

Mg-based storage is unlikely to provide a universal solution for all hydrogen applications. Its strongest opportunities may occur where high volumetric capacity, low storage pressure, and access to suitable heat can compensate for the thermal demands of hydride operation. Stationary storage, integrated industrial systems, and selected transport routes are therefore more credible near-term targets than unrestricted application across the hydrogen economy.

Author Contributions

Y.Z. conceived the review and wrote the manuscript. Y.Z., Y.L., B.W., and J.N. investigated the literature. Y.Z. and Y.L. prepared the figures. X.L., Z.H., B.M., and J.Z. supervised the work. W.D. and J.Z. managed the project. A.C.F. and J.Z. reviewed and edited the manuscript. All authors have read and approved the final version of the manuscript.

Acknowledgements

This work was supported by National Natural Science Foundation of China (52401386), National Key R&D Program of China (2023YFB3809103), Special Fund Project of Jiangsu Province for Scientific and Technological Innovation in Carbon Peaking and Carbon Neutrality (BT2024002). The authors also appreciate the support from the Centre of Hydrogen Science, Shanghai Jiao Tong University, Cambridge Graphene Centre, and Inner Mongolia University of Science and Technology.

Conflicts of Interest

The authors declare no conflicts of interest.

Data Availability Statement

The data that support the findings of this study are available from the corresponding author upon reasonable request.

References

1. R. Sorkhabi, "Energy's international history and future Energy's History: Toward a Global CanonEdited by Daniela Russ and Thomas Turnbull Stanford University Press, 2025. 292 pp," *Science* 388, no. 6748 (2025): 711, https://doi.org/10.1126/science.ady0842.

2. T. M. Lenton, C. Xu, J. F. Abrams, et al., "Quantifying the human Cost of Global Warming," *Nature Sustainability* 6, no. 10 (2023): 1237–1247, https://doi.org/10.1038/s41893-023-01132-6.

3. E. Kearns, R. E. Siegel, D. M. D'Alessandro, J.-W. Lee, and L. A. Berben, "Opportunities for the Renewable Energy Transition via Reactive Carbon Capture," *Chemical Society Reviews* 54, no. 9 (2025): 4096–4103, https://doi.org/10.1039/d4cs00741g.

4. E. L. Clark, "Enhancing Carbon Utilization," *Nature Energy* 8, no. 2 (2023): 119–120, https://doi.org/10.1038/s41560-023-01207-w.

5. A. G. Olabi and M. A. Abdelkareem, "Renewable Energy and Climate Change," *Renewable and Sustainable Energy Reviews* 158 (2022): 112111, https://doi.org/10.1016/j.rser.2022.112111.

6. L. Schlapbach and A. Züttel, "Hydrogen-Storage Materials for Mobile Applications," *Nature* 414, no. 6861 (2001): 353–358, https://doi.org/10.1038/35104634.

7. D. Guan, B. Wang, J. Zhang, et al., "Hydrogen Society: From Present to Future," *Energy & Environmental Science* 16, no. 11 (2023): 4926–4943, https://doi.org/10.1039/d3ee02695g.

8. Z. Chen, S. Mao, W. Hu, Y. Wang, B. Han, and Y. Wang, "From Molecular Hydrogen to Reactive Hydrogen: Activation Pathways and Species Variation in Thermal Catalytic Heterogeneous Hydrogenation," *Chemical Society Reviews* 55, no. 5 (2026): 2831–2875, https://doi.org/10.1039/d5cs00680e.

9. J. O. Abe, A. P. I. Popoola, E. Ajenifuja, and O. M. Popoola, "Hydrogen Energy, Economy and Storage: Review and Recommendation," *International Journal of Hydrogen Energy* 44, no. 29 (2019): 15072–15086, https://doi.org/10.1016/j.ijhydene.2019.04.068.

10. N. Johnson, M. Liebreich, D. M. Kammen, P. Ekins, R. McKenna, and I. Staffell, "Realistic Roles for Hydrogen in the Future Energy Transition," *Nature Reviews Clean Technology* 1, no. 5 (2025): 351–371, https://doi.org/10.1038/s44359-025-00050-4.

15214095, 0, Downloaded from https://advanced.onlinelibrary.wiley.com/doi/10.1002/adma.75618 by Cambridge University Library, Wiley Online Library on [05/11/2026]. See the Terms and Conditions (https://onlinelibrary.wiley.com/terms-and-conditions) on Wiley Online Library for rules of use; OA articles are governed by the applicable Creative Commons License

11. Z. Ouyang, R. B. Jackson, M. Saunois, et al., "The Global Hydrogen Budget," *Nature* 648, no. 8094 (2025): 616–624, https://doi.org/10.1038/s41586-025-09806-1.

12. J. Brandt, T. Iversen, C. Eckert, et al., "Cost and Competitiveness of Green Hydrogen and the Effects of the European Union Regulatory Framework," *Nature Energy* 9, no. 6 (2024): 703–713, https://doi.org/10.1038/s41560-024-01511-z.

13. S. O. Bade and O. S. Tomomewo, "A Review of Governance Strategies, Policy Measures, and Regulatory Framework for Hydrogen Energy in the United States," *International Journal of Hydrogen Energy* 78 (2024): 1363–1381, https://doi.org/10.1016/j.ijhydene.2024.06.338.

14. P. M. Falcone, M. Hiete, and A. Sapio, "Hydrogen Economy and Sustainable Development Goals: Review and Policy Insights," *Current Opinion in Green and Sustainable Chemistry* 31 (2021): 100506, https://doi.org/10.1016/j.cogsc.2021.100506.

15. C. Gunathilake, I. Soliman, D. Panthi, et al., "A Comprehensive Review on Hydrogen Production, Storage, and Applications," *Chemical Society Reviews* 53, no. 22 (2024): 10900–10969, https://doi.org/10.1039/d3cs00731f.

16. M. R. Usman, "Hydrogen Storage Methods: Review and Current Status," *Renewable and Sustainable Energy Reviews* 167 (2022): 112743, https://doi.org/10.1016/j.rser.2022.112743.

17. R. Nagar, S. Srivastava, S. L. Hudson, et al., "Recent Developments in state-of-the-art Hydrogen Energy Technologies—Review of Hydrogen Storage Materials," *Solar Compass* 5 (2023): 100033, https://doi.org/10.1016/j.solcom.2023.100033.

18. M. D. Allendorf, V. Stavila, J. L. Snider, et al., "Challenges to Developing Materials for the Transport and Storage of Hydrogen," *Nature Chemistry* 14, no. 11 (2022): 1214–1223, https://doi.org/10.1038/s41557-022-01056-2.

19. P. Gao, X. Zhang, X. Hu, et al., "Li/Mg-Based Hydrides for High-Capacity Hydrogen and Lithium Storage Applications," *Advanced Functional Materials* 35, no. 46 (2025): 2425155, https://doi.org/10.1002/adfm.202425155.

20. D. Khan and W. J. Ong, "Tailoring Hydrogen Storage Materials Kinetics and Thermodynamics Through Nanostructuring, and Nanoconfinement With In-Situ Catalysis," *Interdisciplinary Materials* 4, no. 2 (2025): 249–283, https://doi.org/10.1002/idm2.12234.

21. A. Reiser, B. Bogdanović, and K. Schlichte, "The Application of Mg-Based Metal-Hydrides as Heat Energy Storage Systems," *International Journal of Hydrogen Energy* 25, no. 5 (2000): 425–430, https://doi.org/10.1016/s0360-3199(99)00057-9.

22. Y. Liu, M. Yue, Y. Guo, et al., "Catalytic Effect of Carbon-Supported NiCoFeCuMg High-Entropy Alloy Nanocatalysts on Hydrogen Storage Properties of MgH_2," *Journal of Magnesium and Alloys* 13, no. 3 (2025): 1232–1242, https://doi.org/10.1016/j.jma.2024.04.031.

23. S. Guan, S. Shen, Y. Dou, et al., "Progress and Perspectives on Hydrogen Storage and Release in the Negative Hydrogen Medium," *Energy & Environmental Science* 18, no. 21 (2025): 9324–9372, https://doi.org/10.1039/d5ee04149j.

24. Y. Yang, W.-G. Cui, Y. Yang, et al., "Thermodynamic Modification of Mg-Based Hydrogen Storage Alloys: Strategies, Mechanisms, and Prospects," *Renewable and Sustainable Energy Reviews* 240 (2026): 117189, https://doi.org/10.1016/j.rser.2026.117189.

25. L. I. Ren, Y. Li, N. Zhang, et al., "Nanostructuring of Mg-Based Hydrogen Storage Materials: Recent Advances for Promoting Key Applications," *Nano-Micro Letters* 15, no. 1 (2023): 93, https://doi.org/10.1007/s40820-023-01041-5.

26. J. Zhang, M. Liu, J. Qi, et al., "Advanced Mg-Based Materials for Energy Storage: Fundamental, Progresses, Challenges and Perspectives," *Progress in Materials Science* 148 (2025): 101381, https://doi.org/10.1016/j.pmatsci.2024.101381.

27. R. Bardhan, A. M. Ruminski, A. Brand, and J. J. Urban, "Magnesium Nanocrystal-Polymer Composites: A New Platform for Designer Hydrogen Storage Materials," *Energy & Environmental Science* 4, no. 12 (2011): 4882, https://doi.org/10.1039/c1ee02258j.

28. Y. Li, Q. Zhang, L. Ren, et al., "Core–Shell Nanostructured Magnesium-Based Hydrogen Storage Materials: A Critical Review," *Industrial Chemistry & Materials* 1, no. 3 (2023): 282–298, https://doi.org/10.1039/d3im00061c.

29. J. F. Stampfer, C. E. Holley, and J. F. Suttle, "The Magnesium-Hydrogen System1-3," *Journal of the American Chemical Society* 82, no. 14 (1960): 3504–3508, https://doi.org/10.1021/ja01499a006.

30. K. S. Nivedhitha, T. Beena, N. R. Banapurmath, et al., "Advances in Hydrogen Storage With Metal Hydrides: Mechanisms, Materials, and Challenges," *International Journal of Hydrogen Energy* 61 (2024): 1259–1273, https://doi.org/10.1016/j.ijhydene.2024.02.335.

31. K. Reddad, H. Labrim, and R. E. Bouayadi, "Predictive Modeling of Temperature Programmed Desorption (TPD) in Magnesium Hydride MgH_2," *Fuel* 403 (2026): 136152, https://doi.org/10.1016/j.fuel.2025.136152.

32. A. Gupta, G. V. Baron, P. Perreault, et al., "Hydrogen Clathrates: Next Generation Hydrogen Storage Materials," *Energy Storage Materials* 41 (2021): 69–107, https://doi.org/10.1016/j.ensm.2021.05.044.

33. L. Dan, H. Wang, X. Yang, J. Liu, L. Ouyang, and M. Zhu, "Low-Temperature Solid-State Hydrogen Storage via Efficiently Catalyzed MgH_2," *Renewable Energy* 231 (2024): 121009, https://doi.org/10.1016/j.renene.2024.121009.

34. J. Čermák and L. Král, "Hydrogen Diffusion in Mg-H and Mg-Ni-H Alloys," *Acta Materialia* 56 (2008): 2677–2686, https://doi.org/10.1016/j.actamat.2008.02.003.

35. Y. Liu, J. Wang, C. Wei, L. Zhang, B. Han, and Y. Du, "Revealing the Effects of NbH_x (x = 1, 2)/MgH_2 Interfaces on the Dehydrogenation of MgH_2 From First-Principles," *Journal of Materials Chemistry A* 14, no. 15 (2026): 8999–9009, https://doi.org/10.1039/d5ta07843a.

36. J. Lyu, V. Kudiiarov, and A. Lider, "Experimentally Observed Nucleation and Growth Behavior of Mg/MgH_2 During De/Hydrogenation of MgH_2/Mg: A Review," *Materials* 15, no. 22 (2022): 8004, https://doi.org/10.3390/ma15228004.

37. D. P. Broom, *Hydrogen Storage Materials: The Characterisation of Their Storage Properties* (Springer, 2011), https://doi.org/10.1007/978-0-85729-221-6.

38. Q. Li, S. Qiu, C. Wu, K. T. Lau, C. Sun, and B. Jia, "Computational Investigation of MgH_2/Graphene Heterojunctions for Hydrogen Storage," *Journal of Physical Chemistry C* 125, no. 4 (2021): 2357–2363, https://doi.org/10.1021/acs.jpcc.0c10714.

39. Y. Wang, M. Liu, T. Zhang, F. Kong, and J. Zheng, "Synergistic Catalysis of Biomass-Derived Porous Carbon Decorated With Cobalt Fluoride on the Hydrogen Storage Properties of MgH_2–$NaBH_4$ Composite," *International Journal of Hydrogen Energy* 217 (2026): 153945, https://doi.org/10.1016/j.ijhydene.2026.153945.

40. Q. Shi, R. Bai, C. Zhang, et al., "Facet-Engineered Anatase TiO_2 Nanoflowers With Anchored Single-Atom Pd for Ultrafast Hydrogen Storage Kinetics," *Advanced Energy Materials* 16 (2026): 05141, https://doi.org/10.1002/aenm.202505141.

41. X. Hu, Y. Pang, C. Li, et al., "Hydrogen Storage of Mg Under an Ultralow Pressure of 1 Bar," *SusMat* 5, no. 6 (2025): 70048, https://doi.org/10.1002/sus2.70048.

42. J. de Jesús Vega-Soria, E. D. Ruiz-Santacruz, N. L. Torres-García, et al., "Systematic Study of First-Row Transition Metals Chlorides as Reaction Accelerators for Mg/MgH_2 for Hydrogen Storage Application," *International Journal of Hydrogen Energy* 141 (2025): 979–995, https://doi.org/10.1016/j.ijhydene.2024.09.440.

43. T. Zhang, M. Liu, C. Li, et al., "Synergistic Catalysis of YF_3 and Ni/C: Exceptional Effects on Hydrogen Storage Performances of MgH_2 at Low

15214095, 0, Downloaded from https://advanced.onlinelibrary.wiley.com/doi/10.1002/adma.75618 by Cambridge University Library, Wiley Online Library on [05/11/2026]. See the Terms and Conditions (https://onlinelibrary.wiley.com/terms-and-conditions) on Wiley Online Library for rules of use; OA articles are governed by the applicable Creative Commons License

Temperature," *Chemical Engineering Journal* 511 (2025): 162185, https://doi.org/10.1016/j.cej.2025.162185.

44. T. Huang, X. U. Huang, C. Hu, et al., "MOF-derived Ni Nanoparticles Dispersed on Monolayer MXene as Catalyst for Improved Hydrogen Storage Kinetics of MgH," *Chemical Engineering Journal* 421 (2021): 127851, https://doi.org/10.1016/j.cej.2020.127851.

45. B. Zhang, X. Xie, Y. Wang, et al., "In Situ Formation of Multiple Catalysts for Enhancing the Hydrogen Storage of MgH_2 by Adding Porous $Ni_3ZnC_0.7$/Ni Loaded Carbon Nanotubes Microspheres," *Journal of Magnesium and Alloys* 12, no. 3 (2024): 1227–1238, https://doi.org/10.1016/j.jma.2022.07.004.

46. J. Wu, Z. Liu, H. Zhang, et al., "Hydrogen Storage Performance of MgH_2 Under Catalysis by Highly Dispersed Nickel-Nanoparticle–Doped Hollow Spherical Vanadium Nitride," *Journal of Magnesium and Alloys* 12, no. 12 (2024): 5132–5143, https://doi.org/10.1016/j.jma.2023.11.010.

47. F.-F. Hong, W.-T. Shi, R.-L. Zhao, et al., "Improvement in Hydrogen Storage Performance of MgH2by Vanadium Doped With ZIF-8 Derived a Single-Atom Catalyst V–N–C," *Rare Metals* 43, no. 6 (2024): 2623–2635, https://doi.org/10.1007/s12598-024-02639-3.

48. J.-Y. Sui, W. Jiang, N. Si, Z. Wang, and Z. Cao, "Hydrogen Storage Kinetics of $TiH_2/ZrCl_4$ Catalyst Based on MgH_2," *International Journal of Hydrogen Energy* 134 (2025): 10–17, https://doi.org/10.1016/j.ijhydene.2025.04.520.

49. M. U. Rahman, M. F. Elsadek, R. Roopashree, and A. Kashyap, "Advancing Hydrogen Storage and Exploring the Potential of Perovskite Hydrides and Metal Hydrides," *Reviews in Inorganic Chemistry* 46, no. 2 (2026): 267–284, https://doi.org/10.1515/revic-2025-0006.

50. J. Zhang, H. Qu, S. Yan, G. Wu, X. F. Yu, and P. Peng, "Enhanced Hydrogen Diffusion in Magnesium Based Hydride Induced by Strain and Doping From First Principle Study," *Journal of Alloys and Compounds* 694 (2017): 687–693, https://doi.org/10.1016/j.jallcom.2016.10.058.

51. C. Liu, Z. Yuan, W. Li, T. Zhai, Z. Han, and X. Zhang, "Improved Hydrogen Storage Performance of MgH_2 by Adding CeO_2@NC With High Catalytic Activity," *Journal of Materials Science & Technology* 238 (2025): 119–131, https://doi.org/10.1016/j.jmst.2025.02.066.

52. D. Feng, H. Li, D. Li, L. Zhang, Z. Yuan, and Y. Zhang, "Enhanced Hydrogen Storage Properties of MgH_2 Catalyzed by TiVCrFeNi High Entropy Alloy," *Journal of Alloys and Compounds* 1043 (2025): 184150, https://doi.org/10.1016/j.jallcom.2025.184150.

53. A. J. Du, S. C. Smith, X. D. Yao, and G. Q. Lu, "Hydrogen Spillover Mechanism on a Pd-Doped Mg Surface as Revealed by Ab Initio Density Functional Calculation," *Journal of the American Chemical Society* 129, no. 33 (2007): 10201–10204, https://doi.org/10.1021/ja0722776.

54. N. Patelli, A. Migliori, V. Morandi, and L. Pasquini, "Interfaces Within Biphasic Nanoparticles Give a Boost to Magnesium-based Hydrogen Storage," *Nano Energy* 72 (2020): 104654, https://doi.org/10.1016/j.nanoen.2020.104654.

55. J. Zang, S. Wang, R. Hu, et al., "Ni, Beyond Thermodynamic Tuning, Maintains the Catalytic Activity of V Species in $Ni_3(VO_4)_2$ Doped MgH_2," *Journal of Materials Chemistry A* 9, no. 13 (2021): 8341–8349, https://doi.org/10.1039/d0ta12079k.

56. J. Cui, J. Liu, H. Wang, et al., "Mg–TM (TM: Ti, Nb, V, Co, Mo or Ni) Core–Shell Like nanostructures: Synthesis, Hydrogen Storage Performance and Catalytic Mechanism," *Journal of Materials Chemistry A* 2 (2014): 9645–9655, https://doi.org/10.1039/c4ta00221k.

57. H. Yu, Z. Yuan, Q. Han, J. Li, and T. Li, "Magnesium-based Hydrogen Storage Materials: Design and Performance Optimization of Single-Component and Multi-Component Systems Review," *International Journal of Hydrogen Energy* 211 (2026): 153673, https://doi.org/10.1016/j.ijhydene.2026.153673.

58. L. Li, Z. Zhang, L. Jiao, H. Yuan, and Y. Wang, "In Situ Preparation of Nanocrystalline Ni@C and its Effect on Hydrogen Storage Properties of MgH_2," *International Journal of Hydrogen Energy* 41, no. 40 (2016): 18121–18129, https://doi.org/10.1016/j.ijhydene.2016.07.170.

59. X. Huang, X. Xiao, W. Zhang, et al., "Transition Metal (Co, Ni) Nanoparticles Wrapped With Carbon and Their Superior Catalytic Activities for the Reversible Hydrogen Storage of Magnesium Hydride," *Physical Chemistry Chemical Physics* 19, no. 5 (2017): 4019–4029, https://doi.org/10.1039/c6cp07852d.

60. Q. Meng, Y. Huang, J. Ye, et al., "Electrospun Carbon Nanofibers With In-Situ Encapsulated Ni Nanoparticles as Catalyst for Enhanced Hydrogen Storage of MgH_2," *Journal of Alloys and Compounds* 851 (2021): 156874, https://doi.org/10.1016/j.jallcom.2020.156874.

61. Y. Zhao, Z. Liu, J. Liu, et al., "Improvement Effect of Reversible Solid Solutions $Mg_2Ni(Cu)/Mg_2Ni(Cu)H_4$ on Hydrogen Storage Performance of MgH2," *Journal of Magnesium and Alloys* 12, no. 1 (2024): 197–208, https://doi.org/10.1016/j.jma.2022.04.006.

62. H. Li, D. Feng, H. Gao, et al., "Bidirectional synergistic catalysis in Y_2O_3-Doped VCrMnFeNi High-Entropy alloy for efficient hydrogen storage of MgH_2," *International Journal of Hydrogen Energy* 171 (2025): 151282, https://doi.org/10.1016/j.ijhydene.2025.151282.

63. Y. Zheng, L. Zhang, H. Zheng, et al., "Catalytic Effects of Multiple Heterointerfaces on the Hydrogen Storage Properties of Magnesium Hydride," *Journal of Colloid and Interface Science* 685 (2025): 65–72, https://doi.org/10.1016/j.jcis.2025.01.100.

64. H. Wan, X. Yang, S. Zhou, et al., "Enhancing Hydrogen Storage Properties of MgH_2 Using FeCoNiCrMn High Entropy Alloy Catalysts," *Journal of Materials Science & Technology* 149 (2023): 88–98, https://doi.org/10.1016/j.jmst.2022.11.033.

65. Y. Liu, C. Wang, Y. Song, et al., "Reduced Graphene Oxide/Patronite Composite as Highly Active Catalyst Precursors for Enhancing the Hydrogen Desorption of MgH_2," *Journal of Magnesium and Alloys* 13, no. 9 (2025): 4596–4609, https://doi.org/10.1016/j.jma.2025.03.014.

66. N. Xu, K. Wang, Y. Zhu, and Y. Zhang, "PdNi Biatomic Clusters from Metallene Unlock Record-Low Onset Dehydrogenation Temperature for Bulk-MgH_2," *Advanced Materials* 35, no. 38 (2023): 2303173, https://doi.org/10.1002/adma.202303173.

67. X. Ding, J. Ding, W. Cao, et al., "Collaborative Optimization of Hydrogen Storage Properties via Self-Formation of Bimetallic Oxide and Electron Buffering of Sc: An Air-Stable MgSc-TiO_2 Composites," *Advanced Functional Materials* 36 (2026): 76138, https://doi.org/10.1002/adfm.76138.

68. W. Hu, J. Zang, Q. Wang, et al., "Spring Effect Endowing P-doped Li_3VO_4 With Long-standing Catalytic Activity for Tuning Cycling Stability of MgH_2," *Advanced Energy Materials* 15, no. 7 (2025): 2404650, https://doi.org/10.1002/aenm.202404650.

69. B. Jia, J. Zhang, X. Chen, et al., "Electronic Structure Modulation of Nb_2O_5 by Ru Single Atoms Enabling Efficient Hydrogen Storage of Magnesium Hydrides," *Angewandte Chemie International Edition* 64, no. 33 (2025): 202511139, https://doi.org/10.1002/anie.202511139.

70. L. Ren, Y. Li, Z. Li, et al., "Boosting Hydrogen Storage Performance of MgH_2 by Oxygen Vacancy-Rich H-V_2O_5 Nanosheet as an Excited H-Pump," *Nano-Micro Letters* 16, no. 1 (2024): 160, https://doi.org/10.1007/s40820-024-01375-8.

71. X. L. Zhang, Y. F. Liu, X. Zhang, J. J. Hu, M. X. Gao, and H. G. Pan, "Empowering Hydrogen Storage Performance of MgH_2 by Nanoengineering and Nanocatalysis," *Materials Today Nano* 9 (2020): 100064, https://doi.org/10.1016/j.mtnano.2019.100064.

72. D. R. Leiva, A. M. Jorge, T. T. Ishikawa, et al., "Nanoscale Grain Refinement and H-Sorption Properties of MgH_2 Processed by High-Pressure Torsion and Other Mechanical Routes," *Advanced Engineering Materials* 12, no. 8 (2010): 786–792, https://doi.org/10.1002/adem.201000030.

73. C. Zhu, S. Hosokai, and T. Akiyama, "Direct Synthesis of MgH_2 Nanofibers From Waste Mg," *International Journal of Hydrogen Energy* 37, no. 10 (2012): 8379–8387, https://doi.org/10.1016/j.ijhydene.2012.02.085.

15214095, 0, Downloaded from https://advanced.onlinelibrary.wiley.com/doi/10.1002/adma.75618 by Cambridge University Library, Wiley Online Library on [05/11/2026]. See the Terms and Conditions (https://onlinelibrary.wiley.com/terms-and-conditions) on Wiley Online Library for rules of use; OA articles are governed by the applicable Creative Commons License

74. J. Huot, G. Liang, S. Boily, A. Van Neste, and R. Schulz, "Structural Study and Hydrogen Sorption Kinetics of Ball-Milled Magnesium Hydride," *Journal of Alloys and Compounds* 293–295 (1999): 495–500, https://doi.org/10.1016/s0925-8388(99)00474-0.

75. N. S. Norberg, T. S. Arthur, S. J. Fredrick, and A. L. Prieto, "Size-Dependent Hydrogen Storage Properties of Mg Nanocrystals Prepared From Solution," *Journal of the American Chemical Society* 133, no. 28 (2011): 10679–10681, https://doi.org/10.1021/ja201791y.

76. J. J. Liang and W. C. P. Kung, "Confinement of Mg−MgH_2 Systems Into Carbon Nanotubes Changes Hydrogen Sorption Energetics," *Journal of Physical Chemistry B* 109, no. 38 (2005): 17837–17841, https://doi.org/10.1021/jp052134a.

77. A. Schneemann, J. L. White, S. Kang, et al., "Nanostructured Metal Hydrides for Hydrogen Storage," *Chemical Reviews* 118, no. 22 (2018): 10775–10839, https://doi.org/10.1021/acs.chemrev.8b00313.

78. R. W. P. Wagemans, J. H. van Lenthe, P. E. de Jongh, A. J. van Dillen, and K. P. de Jong, "Hydrogen Storage in Magnesium Clusters: Quantum Chemical Study," *Journal of the American Chemical Society* 127, no. 47 (2005): 16675–16680, https://doi.org/10.1021/ja054569h.

79. W. Li, C. Li, H. Ma, and J. Chen, "Magnesium Nanowires: Enhanced Kinetics for Hydrogen Absorption and Desorption," *Journal of the American Chemical Society* 129, no. 21 (2007): 6710–6711, https://doi.org/10.1021/ja071323z.

80. X. Zhang, Y. Liu, Z. Ren, et al., "Realizing 6.7 wt% Reversible Storage of Hydrogen at Ambient Temperature With Non-Confined Ultrafine Magnesium Hydrides," *Energy & Environmental Science* 14, no. 4 (2021): 2302–2313, https://doi.org/10.1039/d0ee03160g.

81. L. I. Ren, W. Zhu, Q. Zhang, et al., "MgH_2 Confinement in MOF-Derived N-Doped Porous Carbon Nanofibers for Enhanced Hydrogen Storage," *Chemical Engineering Journal* 434 (2022): 134701, https://doi.org/10.1016/j.cej.2022.134701.

82. M. Liu, S. Zhao, X. Xiao, et al., "Novel 1D Carbon Nanotubes Uniformly Wrapped Nanoscale MgH_2 for Efficient Hydrogen Storage Cycling Performances With Extreme High Gravimetric and Volumetric Capacities," *Nano Energy* 61 (2019): 540–549, https://doi.org/10.1016/j.nanoen.2019.04.094.

83. G. Xia, Y. Tan, X. Chen, et al., "Monodisperse Magnesium Hydride Nanoparticles Uniformly Self-Assembled on Graphene," *Advanced Materials* 27, no. 39 (2015): 5981–5988, https://doi.org/10.1002/adma.201502005.

84. W. Zhu, L. Ren, C. Lu, et al., "Nanoconfined and in Situ Catalyzed MgH_2 Self-Assembled on 3D Ti_3C_2 MXene Folded Nanosheets With Enhanced Hydrogen Sorption Performances," *ACS Nano* 15, no. 11 (2021): 18494–18504, https://doi.org/10.1021/acsnano.1c08343.

85. L. Ren, W. Zhu, Y. Li, et al., "Oxygen Vacancy-Rich 2D TiO_2 Nanosheets: A Bridge Toward High Stability and Rapid Hydrogen Storage Kinetics of Nano-Confined MgH_2," *Nano-Micro Letters* 14, no. 1 (2022): 144, https://doi.org/10.1007/s40820-022-00891-9.

86. H. Lu, J. Li, R. Zhang, et al., "Advances and Perspectives of Two-Dimensional Materials MXenes: Efficient Catalysts for Magnesium Hydride," *Renewable and Sustainable Energy Reviews* 217 (2025): 115759, https://doi.org/10.1016/j.rser.2025.115759.

87. Y. Zhao, B. Wang, L. Ren, et al., "Nanostructured MXene-Based Materials for Boosting Hydrogen Sorption Properties of Mg/MgH_2," *Materials Reports: Energy* 4, no. 1 (2024): 100255, https://doi.org/10.1016/j.matre.2024.100255.

88. Y. Li, L. Ren, Y. Yao, et al., "A Single-Atom Interface Engineering Strategy to Promote Hydrogen Sorption Performances of Magnesium Hydride," *Advanced Functional Materials* 35, no. 13 (2025): 2417915, https://doi.org/10.1002/adfm.202417915.

89. Y. Li, L. I. Ren, Z. I. Li, et al., "Achieving Wide-Temperature-Range Physical and Chemical Hydrogen Sorption in a Structural Optimized Mg/N-Doped Porous Carbon Nanocomposite," *Nano-Micro Letters* 18, no. 1 (2026): 94, https://doi.org/10.1007/s40820-025-01931-w.

90. Z. Ma, S. Panda, Q. Zhang, et al., "Improving Hydrogen Sorption Performances of MgH_2 Through Nanoconfinement in a Mesoporous CoS Nano-Boxes Scaffold," *Chemical Engineering Journal* 406 (2021): 126790, https://doi.org/10.1016/j.cej.2020.126790.

91. X. Xing, Y. Wang, Z. Zhang, et al., "$MgBu_2$ Nanosheets Encapsulated in ZIF-8 for Producing Carbon Scaffold in Situ Nanoconfined Mg Hydrogen Storage Materials: Record-High Loading and Decreased Dehydrogenation Enthalpy," *Nano Energy* 127 (2024): 109740, https://doi.org/10.1016/j.nanoen.2024.109740.

92. T. Noritake, S. Towata, M. Aoki, et al., "Charge Density Measurement in MgH_2 by Synchrotron X-Ray Diffraction," *Journal of Alloys and Compounds* 356–357 (2003): 84–86, https://doi.org/10.1016/s0925-8388(03)00104-x.

93. W. Wang, L. Bao, H. Yan, et al., "First-Principle Study on the Adsorption Behavior and Bonding Characteristics of Hydrogen on Mg Low-Index Surfaces," *Computational Materials Science* 260 (2025): 114216, https://doi.org/10.1016/j.commatsci.2025.114216.

94. D. Zhou, C. Zheng, Y. Zhang, et al., "An Overview of RE-Mg-based Alloys for Hydrogen Storage: Structure, Properties, Progresses and Perspectives," *Journal of Magnesium and Alloys* 13, no. 1 (2025): 41–70, https://doi.org/10.1016/j.jma.2024.12.020.

95. X. Lu, L. Zhang, J. Zheng, and X. Yu, "Construction of Carbon Covered Mg_2NiH_4 Nanocrystalline for Hydrogen Storage," *Journal of Alloys and Compounds* 5, no. 905 (2022): 164169, https://doi.org/10.1016/j.jallcom.2022.164169.

96. J. J. Reilly and R. H. Wiswall, "Reaction of Hydrogen With Alloys of Magnesium and Nickel and the Formation of Mg_2NiH_4," *Inorganic Chemistry* 7, no. 11 (1968): 2254–2256, https://doi.org/10.1021/ic50069a016.

97. H. Yong, S. Guo, Z. Yuan, Y. Qi, D. Zhao, and Y. Zhang, "Catalytic Effect of in Situ Formed Mg_2Ni and REH (RE: Ce and Y) on Thermodynamics and Kinetics of Mg-RE-Ni Hydrogen Storage Alloy," *Renewable Energy* 157 (2020): 828–839, https://doi.org/10.1016/j.renene.2020.05.043.

98. W. R. Myers, L.-W. Wang, T. J. Richardson, and M. D. Rubin, "Calculation of Thermodynamic, Electronic, and Optical Properties of Monoclinic Mg_2NiH_4," *Journal of Applied Physics* 91, no. 8 (2002): 4879–4885, https://doi.org/10.1063/1.1454206.

99. A. Assila, M. Rkhis, A. Alaoui-Belghiti, et al., "Feeling the Strain: Enhancing the Thermodynamics Characteristics of Magnesium Nickel Hydride Mg_2NiH_4 for Hydrogen Storage Applications Through Strain Engineering," *International Journal of Hydrogen Energy* 67 (2024): 651–657, https://doi.org/10.1016/j.ijhydene.2024.04.159.

100. Y. Zhao, Y. Zhu, R. Shi, et al., "Magnesium Nickel Hydride Monocrystalline Nanoparticles for Reversible Hydrogen Storage," *Materials Reports: Energy* 4, no. 1 (2024): 100246, https://doi.org/10.1016/j.matre.2023.100246.

101. E. Rönnebro, J. O. Jensen, D. Noréus, and N. J. Bjerrum, "Structural Studies of Disordered Mg_2NiH_4 Formed by Mechanical Grinding," *Journal of Alloys and Compounds* 293–295 (1999): 146–149, https://doi.org/10.1016/s0925-8388(99)00315-1.

102. J. Zhang, Y. Zhu, H. Lin, et al., "Metal Hydride Nanoparticles With Ultrahigh Structural Stability and Hydrogen Storage Activity Derived From Microencapsulated Nanoconfinement," *Advanced Materials* 29, no. 24 (2017): 1700760, https://doi.org/10.1002/adma.201700760.

103. Y. Zhao, Y. Zhu, R. Shi, et al., "Structural Inhomogeneity: A Potential Strategy to Improve the Hydrogen Storage Performance of Metal Hydrides," *Journal of Materials Chemistry A* 11, no. 25 (2023): 13255–13265, https://doi.org/10.1039/d3ta02114a.

104. X. Liu, S. Wu, X. Cai, and L. Zhou, "Hydrogen Storage Behaviour of Cr- and Mn-Doped Mg_2Ni Alloys Fabricated via High-Energy Ball Milling," *International Journal of Hydrogen Energy* 48, no. 45 (2023): 17202–17215, https://doi.org/10.1016/j.ijhydene.2023.01.180.

105. J. J. Vajo, F. Mertens, C. C. Ahn, R. C. Bowman, and B. Fultz, "Altering Hydrogen Storage Properties by Hydride Destabilization Through Alloy Formation: LiH and MgH 2 Destabilized With Si," *Journal of Physical*

15214095, 0, Downloaded from https://advanced.onlinelibrary.wiley.com/doi/10.1002/adma.75618 by Cambridge University Library, Wiley Online Library on [05/11/2026]. See the Terms and Conditions (https://onlinelibrary.wiley.com/terms-and-conditions) on Wiley Online Library for rules of use; OA articles are governed by the applicable Creative Commons License

Chemistry B 108, no. 37 (2004): 13977–13983, https://doi.org/10.1021/jp040060h.

106. S. Cao, Y. Li, B. Wang, et al., "Low Temperature Thermolysis and Hydrolysis of MgH_2 Generated From a Titanium-Mediated Hydrogenation of Mg_2Si," *Journal of Magnesium and Alloys* 20 (2026): 101809, https://doi.org/10.1016/j.jma.2025.07.002.

107. X. F. Tan, M. Kim, Q. Gu, et al., "Na-Modified Cast Hypo-Eutectic Mg–Mg_2Si Alloys for Solid-State Hydrogen Storage," *Journal of Power Sources* 538 (2022): 231538, https://doi.org/10.1016/j.jpowsour.2022.231538.

108. H. Shao, Y. Wang, H. Xu, and X. Li, "Preparation and Hydrogen Storage Properties of Nanostructured Mg_2Cu Alloy," *Journal of Solid State Chemistry* 178, no. 7 (2005): 2211–2217, https://doi.org/10.1016/j.jssc.2005.04.036.

109. H. Shao, H. Xu, Y. Wang, and X. Li, "Synthesis and Hydrogen Storage Behavior of Mg–Co–H System at Nanometer Scale," *Journal of Solid State Chemistry* 177, no. 10 (2004): 3626–3632, https://doi.org/10.1016/j.jssc.2004.05.003.

110. G. F. de Lima, S. Garroni, M. D. Baró, et al., "Hydrogen Storage Properties of 2Mg-Fe Mixtures Processed by Hot Extrusion: Influence of the Extrusion Ratio," *International Journal of Hydrogen Energy* 37, no. 20 (2012): 15196–15203, https://doi.org/10.1016/j.ijhydene.2012.07.121.

111. B. Bogdanovic, A. Reiser, K. Schlichte, B. Spliethoff, and B. Tesche, "Thermodynamics and Dynamics of the Mg–Fe–H System and its Potential for Thermochemical Thermal Energy Storage," *Journal of Alloys and Compounds* 345, no. 1–2 (2002): 77–89, https://doi.org/10.1016/s0925-8388(02)00308-0.

112. J. Kim, J. O. Fadonougbo, J.-H. Bae, et al., "Real-Time Monitoring of the Dehydrogenation Behavior of a Mg_2FeH_6–MgH_2 Composite by In Situ Transmission Electron Microscopy," *Advanced Functional Materials* 32, no. 39 (2022): 2204147, https://doi.org/10.1002/adfm.202204147.

113. X. Zhang, C. Li, J. Ye, et al., "Light-Enabled Reversible Hydrogen Storage of Borohydrides Activated by Photogenerated Vacancies," *Journal of the American Chemical Society* 147, no. 3 (2025): 2786–2796, https://doi.org/10.1021/jacs.4c15744.

114. A. S. Awad, M. Nakhl, M. Zakhour, S. F. Santos, F. L. Souza, and J.-L. Bobet, "Effect of Microwave Irradiation on Hydrogen Sorption Properties of Hand Mixed MgH_2–10 wt.% Carbon Fibers," *Journal of Alloys and Compounds* 676 (2016): 1–8, https://doi.org/10.1016/j.jallcom.2016.03.008.

115. P. Zhou, L. Zhang, Y. Liu, et al., "Non-Thermal External Field-Driven Synthesis and Performance Modulation of High-Density Hydrogen Storage Materials," *Energy Storage Materials* 82 (2025): 104562, https://doi.org/10.1016/j.ensm.2025.104562.

116. Z. Cheng, Y. Guan, H. Wen, et al., "Light-Driven De/Rehydrogenation of a LiH Surface Under Ambient Conditions," *Journal of Physical Chemistry Letters* 15, no. 25 (2024): 6662–6667, https://doi.org/10.1021/acs.jpclett.4c00874.

117. Q. Liu and L. Z. Wu, "Recent Advances in Visible-Light-Driven Organic Reactions," *National Science Review* 4, no. 3 (2017): 359–380, https://doi.org/10.1093/nsr/nwx039.

118. D. Dougherty and P. J. Herley, "Photodecomposition Kinetics of Alkaline Earth Hydride Powders," *Journal of the Less Common Metals* 73, no. 1 (1980): 97–104, https://doi.org/10.1016/0022-5088(80)90347-1.

119. Y. Sun and K. F. Aguey-Zinsou, "Light-Activated Hydrogen Storage in Mg, LiH and NaAlH4," *ChemPlusChem* 83, no. 10 (2018): 904–908, https://doi.org/10.1002/cplu.201800190.

120. X. Zhang, Y. Sun, S. Ju, et al., "Solar-Driven Reversible Hydrogen Storage," *Advanced Materials* 35, no. 2 (2023): 2206946, https://doi.org/10.1002/adma.202206946.

121. X. Zhang, S. Ju, C. Li, et al., "Atomic Reconstruction for Realizing Stable Solar-Driven Reversible Hydrogen Storage of Magnesium Hydride," *Nature Communications* 15, no. 1 (2024): 2815, https://doi.org/10.1038/s41467-024-47077-y.

122. Y. Zhao, B. Wang, Y. Li, et al., "Developing Oxygen Vacancy Rich Perovskite for Broad-Spectrum-Responsive Photothermal Assisted Photocatalytic Dehydrogenation of MgH_2," *Advanced Energy Materials* 15, no. 47 (2025): 04765, https://doi.org/10.1002/aenm.202504765.

123. Y. Nakamori, M. Matsuo, K. Yamada, T. Tsutaoka, and S. Orimo, "Effects of Microwave Irradiation on Metal Hydrides and Complex Hydrides," *Journal of Alloys and Compounds* 446–447 (2007): 698–702, https://doi.org/10.1016/j.jallcom.2007.03.096.

124. Y. Nakamori, S. I. Orimo, and T. Tsutaoka, "Dehydriding Reaction of Metal Hydrides and Alkali Borohydrides Enhanced by Microwave Irradiation," *Applied Physics Letters* 88, no. 11 (2006): 112104, https://doi.org/10.1063/1.2185079.

125. H. Y. Leng, J. Wei, Q. Li, and K. C. Chou, "Effect of Microwave Irradiation on the Hydrogen Desorption Properties of MgH_2/$LiBH_4$ Composite," *Journal of Alloys and Compounds* 597 (2014): 136–141, https://doi.org/10.1016/j.jallcom.2014.01.205.

126. A. S. Awad, T. Tayeh, M. Nakhl, et al., "Effect of Carbon Type (Graphite, CFs and Diamond) on the Hydrogen Desorption of Mg–C Powder Mixtures Under Microwave Irradiation," *Journal of Alloys and Compounds* 607 (2014): 223–229, https://doi.org/10.1016/j.jallcom.2014.04.027.

127. R. Zou, J. Adedeji Bolarin, G. Lei, et al., "Microwave-Assisted Reduction of Ti Species in MgH_2-TiO_2 Composite and its Effect on Hydrogen Storage," *Chemical Engineering Journal* 450 (2022): 138072, https://doi.org/10.1016/j.cej.2022.138072.

128. B. Wang, Z. Wu, H. Liu, et al., "Low-Energy and Accelerated Hydrogen Release From MgH_2–5 wt% $NaTiO_xH$ Catalyzed Hydrogen Storage Reactor by Graphite Responsive Microwave," *Journal of Magnesium and Alloys* 13, no. 8 (2025): 3864–3879, https://doi.org/10.1016/j.jma.2025.03.002.

129. T. Lookman, Y. Liu, and Z. Gao, "Materials Informatics: Emergence to Autonomous Discovery in the Age of AI," *Advanced Materials* 38, no. 29 (2026): 15941, https://doi.org/10.1002/adma.202515941.

130. B. Xiao, Y. Tang, and Y. Liu, "Integrating Materials Representations Into Feature Engineering in Machine Learning for Crystalline Materials: From Local to Global Chemistry-Structure Information Coupling," *WIREs Computational Molecular Science* 15, no. 4 (2025): 70044, https://doi.org/10.1002/wcms.70044.

131. S. Chakraborty, J. Björk, M. Dahlqvist, J. Rosen, and F. Heintz, "A Survey of AI-Supported Materials Informatics," *Computer Science Review* 59 (2026): 100845, https://doi.org/10.1016/j.cosrev.2025.100845.

132. R. A. Gouvêa, P.-P. De Breuck, T. Pretto, G.-M. Rignanese, and M. J. L. Santos, "Combining Feature-based Approaches With Graph Neural Networks and Symbolic Regression for Synergistic Performance and Interpretability," *npj Computational Materials* 12 (2026): 67, https://doi.org/10.1038/s41524-025-01938-2.

133. R. Murakami, T. T. Sasaki, H. Yoshikawa, et al., "Bayesian Inference for Peak Feature Extraction and Prediction of Material Property in X-Ray Diffraction Data," *Science and Technology of Advanced Materials: Methods* 4, no. 1 (2024): 2384352, https://doi.org/10.1080/27660400.2024.2384352.

134. I. Batatia, P. Benner, Y. Chiang, et al., "A Foundation Model for Atomistic Materials Chemistry," *Journal of Chemical Physics* 163, no. 18 (2025): 184110, https://doi.org/10.1063/5.0297006.

135. A. Angeletti, L. Leoni, D. Massa, L. Pasquini, S. Papanikolaou, and C. Franchini, "Hydrogen Diffusion in Magnesium Using Machine Learning Potentials: A Comparative Study," *npj Computational Materials* 11, no. 1 (2025): 85, https://doi.org/10.1038/s41524-025-01555-z.

136. Z.-C. Wang, J.-Y. Liu, G.-H. Zhang, W.-F. Jia, and Y. Han, "Unraveling Phase-Dependent Hydrogen Diffusion in MgH_2 Using a Deep Potential Framework," *Journal of Alloys and Compounds* 1079 (2026): 189832, https://doi.org/10.1016/j.jallcom.2026.189832.

137. Y. Ding, L. Tong, X. Liu, Y. Liu, and Y. Zhao, "Artificial Intelligence-Driven Innovations in Hydrogen Storage Technology," *Energy & Envi-*

15214095, 0, Downloaded from https://advanced.onlinelibrary.wiley.com/doi/10.1002/adma.75618 by Cambridge University Library, Wiley Online Library on [05/11/2026]. See the Terms and Conditions (https://onlinelibrary.wiley.com/terms-and-conditions) on Wiley Online Library for rules of use; OA articles are governed by the applicable Creative Commons License

ronmental Materials 8, no. 5 (2025): 70041, https://doi.org/10.1002/eem2.70041.

138. C. Lin, B. C. S. Lee, U. Anjum, et al., "Harnessing Physics-Inspired Machine Learning to Design Nanocluster Catalysts for Dehydrogenating Liquid Organic Hydrogen Carriers," *Applied Catalysis B: Environment and Energy* 371 (2025): 125192, https://doi.org/10.1016/j.apcatb.2025.125192.

139. C. Li, W. Yang, H. Liu, et al., "Picturing the Gap Between the Performance and US-DOE's Hydrogen Storage Target: A Data-Driven Model for MgH_2 Dehydrogenation," *Angewandte Chemie International Edition* 63, no. 28 (2024): 202320151, https://doi.org/10.1002/anie.202320151.

140. P. Zhou, Q. Zhou, X. Xiao, et al., "Machine Learning in Solid-State Hydrogen Storage Materials: Challenges and Perspectives," *Advanced Materials* 37, no. 6 (2025): 2413430, https://doi.org/10.1002/adma.202413430.

141. Y. Shang, C. Pistidda, G. Gizer, T. Klassen, and M. Dornheim, "Mg-based Materials for Hydrogen Storage," *Journal of Magnesium and Alloys* 9, no. 6 (2021): 1837–1860, https://doi.org/10.1016/j.jma.2021.06.007.

142. S. Shen, Z. Xu, F. Dong, S. Xu, and B. Yin, "Application of Machine Learning to Thermal Management of Solid-state Hydrogen Storage: A Comprehensive Review," *Renewable and Sustainable Energy Reviews* 223 (2025): 116010, https://doi.org/10.1016/j.rser.2025.116010.

143. M. Hasnain, H. Sezer, and J. H. Mason, "Mathematical Modeling of Heat and Mass Transfer in Metal Hydride Hydrogen Storage Systems: A Comprehensive Review," *Renewable and Sustainable Energy Reviews* 226 (2026): 116294, https://doi.org/10.1016/j.rser.2025.116294.

144. Y. Zhu, M. Tuluhong, Y. Ji, et al., "Thermo-Hydrogen Coupling Characteristics of Mg-Based Hydrogen Storage Materials and Thermal Management," *Energy Storage Materials* 83 (2025): 104720, https://doi.org/10.1016/j.ensm.2025.104720.

145. I. Elosery, "Theory of the Computer Code RET 1 for the Calculation of Space-Time Dependent Temperature and Composition Properties of Metal Hydride Hydrogen Storage Beds," *International Journal of Hydrogen Energy* 8, no. 3 (1983): 191–198, https://doi.org/10.1016/0360-3199(83)90064-2.

146. G. Lucas and W. Richards, "Mathematical Modelling of Hydrogen Storage Systems," *International Journal of Hydrogen Energy* 9, no. 3 (1984): 225–231, https://doi.org/10.1016/0360-3199(84)90123-x.

147. A. Jemni, "Study of Two-Dimensional Heat and Mass Transfer During Desorption in a Metal-Hydrogen Reactor," *International Journal of Hydrogen Energy* 20, no. 11 (1995): 881–891, https://doi.org/10.1016/0360-3199(94)00115-g.

148. M. D. Mat, Y. K. Kaplan, and K. Aldas, "Investigation of Three-Dimensional Heat and Mass Transfer in a Metal Hydride Reactor," *International Journal of Energy Research* 26, no. 11 (2002): 973–986, https://doi.org/10.1002/er.831.

149. X. Lin, C.-L. Yin, L. Ren, et al., "A One- and Three-Dimensional Coupled Model and Simulation Investigation for the Large-Scale Oil-Heating Type Mg-Based Hydrogen Storage Tank," *Chemical Engineering Journal* 472 (2023): 144943, https://doi.org/10.1016/j.cej.2023.144943.

150. L. Shao, X. Lin, L. Bian, et al., "Engineering Control Strategy of Hydrogen Gas Direct-Heating Type Mg-Based Solid state Hydrogen Storage Tanks: A Simulation Investigation," *Applied Energy* 375 (2024): 124134, https://doi.org/10.1016/j.apenergy.2024.124134.

151. L. Shao, X. Lin, X. Yang, et al., "Magnesium-based Hydrogen Storage Tanks: A Review of Research, Development and Simulation Models," *Renewable and Sustainable Energy Reviews* 211 (2025): 115332, https://doi.org/10.1016/j.rser.2025.115332.

152. F. Rostami, Z. Kis, R. Koppelaar, L. Jiménez, and C. Pozo, "Comparative Sustainability Study of Energy Storage Technologies Using Data Envelopment Analysis," *Energy Storage Materials* 48 (2022): 412–438, https://doi.org/10.1016/j.ensm.2022.03.026.

153. X. Wang, L. Shao, S. Hu, et al., "A Techno-Economic Study of Photovoltaic-solid Oxide Electrolysis Cell Coupled Magnesium Hydride-based Hydrogen Storage and Transportation Toward Large-Scale Applications of Green Hydrogen," *Energy & Environmental Science* 17, no. 22 (2024): 8429–8456, https://doi.org/10.1039/d4ee04224g.

15214095, 0, Downloaded from https://advanced.onlinelibrary.wiley.com/doi/10.1002/adma.75618 by Cambridge University Library, Wiley Online Library on [05/11/2026]. See the Terms and Conditions (https://onlinelibrary.wiley.com/terms-and-conditions) on Wiley Online Library for rules of use; OA articles are governed by the applicable Creative Commons License